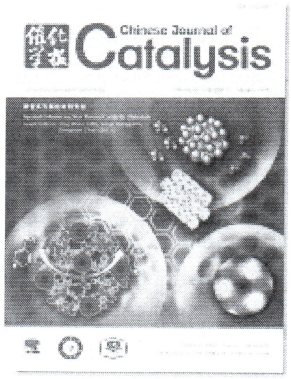

Controlling the Reactions of Free Radicals with Metal-Radical Interaction

Journal:	*Chinese Journal of Catalysis*
Manuscript ID	Draft
Manuscript Type:	Original Article
Date Submitted by the Author:	n/a
Complete List of Authors:	Huang, Zhipeng; Chinese Academy of Sciences Dalian Institute of Chemical Physics Yang, Yang; Chinese Academy of Sciences Dalian Institute of Chemical Physics Mu, Junju; Chinese Academy of Sciences Dalian Institute of Chemical Physics Li, Genheng; Chinese Academy of Sciences Dalian Institute of Chemical Physics Han, Jianyu; Chinese Academy of Sciences Dalian Institute of Chemical Physics Ren, Puning; Chinese Academy of Sciences Dalian Institute of Chemical Physics Zhang, Jian Luo, Nengchao; Chinese Academy of Sciences Dalian Institute of Chemical Physics Han, Ke-Li Wang, Feng; 中国科学院大连化学物理研究所,王峰,
Keyword:	metal-radical interaction, radical reaction, photocatalysis, catalytic mechanism, metal catalyst
Subject:	Reaction kinetics and mechanism, Photocatalysis, Characterization of catalyst and catalytic reaction

Controlling the Reactions of Free Radicals with Metal-Radical Interaction

Zhipeng Huang,[1,2,†] Yang Yang,[3,†] Junju Mu,[1] Genheng Li,[1,4] Jianyu Han,[1,2] Puning Ren,[1,2] Jian Zhang,[1] Nengchao Luo,[1] Ke-Li Han,[3] Feng Wang[1,*]

[1] State Key Laboratory of Catalysis, Dalian National Laboratory for Clean Energy, Dalian Institute of Chemical Physics, Chinese Academy of Sciences, Dalian 116023, China

[2] University of Chinese Academy of Sciences, Beijing 100049, China

[3] State Key Laboratory of Molecular Reaction Dynamics, Dalian Institute of Chemical Physics, Chinese Academy of Sciences, Dalian 116023, China

[4] Zhang Dayu School of Chemistry, Dalian University of Technology, Dalian 116024, China

[†] These authors contributed equally to this work.

*Corresponding author. E-mail: wangfeng@dicp.ac.cn

Abstract

Radicals are key intermediates in numerous reactions. Their high reactivity enables various transformations to occur under mild conditions, however, also brings great challenges to control their reactions especially over heterogeneous catalysts. Here we propose to use metal nanoparticles to directly steer the conversion of free radical species. Results from photocatalytic reactions, *in situ* transient absorption spectroscopy, and theoretical simulation demonstrate that supported Pd nanoparticles can efficiently stabilize free radical species generated from photo-excited TiO_2, and thus manipulate their conversion on catalyst surface, owing to the enhanced electronic interactions between metal and radical species. These understandings are crucial for the design of advanced heterogeneous catalytic systems with controllable radical reactions.

Keywords: Metal-radical interaction, radical reaction, photocatalysis, catalytic mechanism

Introduction

Radicals are key species in chemistry. The intrinsic structures with unpaired electrons render the radical species highly reactive to undergo numerous important transformations, such as coupling reactions for the rapid construction of valuable pharmaceutical molecules and bond scission reactions for renewable biomass valorization [1-3]. Traditionally toxic and hazardous reagents are required to deliver the desired radicals [4-5]. In recent years, the rapid development of photocatalysis has fuelled new energy into radical chemistry as electron transfer between excited photocatalyst and substrate can provide efficient access to active radical intermediates under mild conditions, and in some cases, inexhaustible solar light can be directly used as the driving force [5-6]. The high reactivity, on the other hand, represents great challenges to control the subsequent conversion of active radicals, which necessitates the development of effective catalytic strategies. In homogeneous systems, in addition to a photocatalyst to furnish radical intermediate under irradiation, a second catalytic center (e.g., Ni, Cu, or Pd complex) is usually adapted to manipulate the subsequent conversion of generated radical species to undergo targeted reaction. This strategy, known as dual catalysis or metallaphotocatalysis [7-8], has greatly facilitated the development of many useful protocols for C–C and C–heteroatom bond formation. In contrast, the conversion of radical intermediate is less controllable over heterogeneous photocatalysts. Under irradiation, semiconductor-based photocatalysts, such as TiO_2, can readily activate various substrates into corresponding radical species with photo-generated carriers, but generally play a marginal role in the sequential reaction of radical intermediates [9-10]. That is, generated radical species are prone to react in a free and unspecific manner. They would undergo hydrogen abstraction, dimerization, and

disproportionation reactions, or further oxidize to corresponding cations which would eventually transform into a range of complex products [11]. Manley et al. investigated the homo-coupling of radicals derived from carboxylic acid decarboxylation over TiO_2-based photocatalysts, and found that the product yields varied dramatically with different substrates [12-13], indicating the uncontrollable reactivity of radical species. In order to achieve the selective conversion of radical intermediates, for example, C–C coupling reaction, researchers have to use some delicately designed radical acceptors or a large excess amount of less active coupling agents to kinetically suppress unwanted radical side-reactions [12, 14-16], which limits the further development of heterogeneous photocatalysis for practical applications. In this context, the fabrication of catalytic sites on semiconductor to directly manipulate the reactivity of key radical intermediate would be favorable.

The interaction between metal catalyst and radical species is an important topic in catalysis. The chemistry of hydrocarbon radicals chemisorbed on metal has been thoroughly investigated in surface science, which provides comprehensive insight into the fundamental processes in petrochemical industry [17-18]. The metal-radical interaction has also been demonstrated to play an important role in the conversions of *in situ* generated radicals on metal center, such as their selective coupling reactions [19-21]. Moreover, Meyerstein and colleagues found that metal nanoparticles can considerably prolong the lifetime of methyl radical generated from γ-irradiation stimulation in aqueous solution [22-23]. Similarly, Zhang et al. reported that persistent nitroxyl radicals are capable of reversibly chemisorbing on gold nanoparticles via electronic interactions between the unpaired electrons and the metallic particles [24]. Inspired by these studies, we envisioned that making use of metal-radical

interaction may provide great opportunities to stabilize active free radical intermediates and subsequently steer their conversion in a controllable manner. However, the ability of metal catalysts to directly intervene the reactions of extraneous radical species, for instance, those generated on the photo-excited semiconductors (the most frequent situation in heterogeneous photocatalysis), remains largely unexplored. In addition, free radicals are known for their high reactivity and short lifetime. For example, the rate constant for homo-coupling of benzyl radical is about 4×10^9 L mol^{-1} s^{-1}, which means it can react in rates close to the diffusion-controlled limit in solution [25]. These features make the feasibility of our proposal to tune the conversion of extraneous free radical with metal catalyst more questionable.

In this article, we devote to studying the interactions between metal catalyst and free radical species, the fundamental issue in heterogeneous catalysis and radical chemistry. The influence of various supported metal catalysts (Pt, Au, Ni, Rh, and Pd) on the conversion of benzyl radical derived from photo-excited TiO_2 was investigated in detail with experimental, spectral and computational methods. Especially, *in situ* transient absorption (TA) spectroscopy revealed the distinct reaction kinetics of active radical species over different metal/TiO_2 catalysts. These combined evidences demonstrate that Pd nanoparticles are able to stabilize extraneous free radicals and control their subsequent conversion, owing to the unique electronic structure of Pd. Such strong metal-radical interaction offers great opportunities to design efficient heterogeneous catalysts for selective radical reactions.

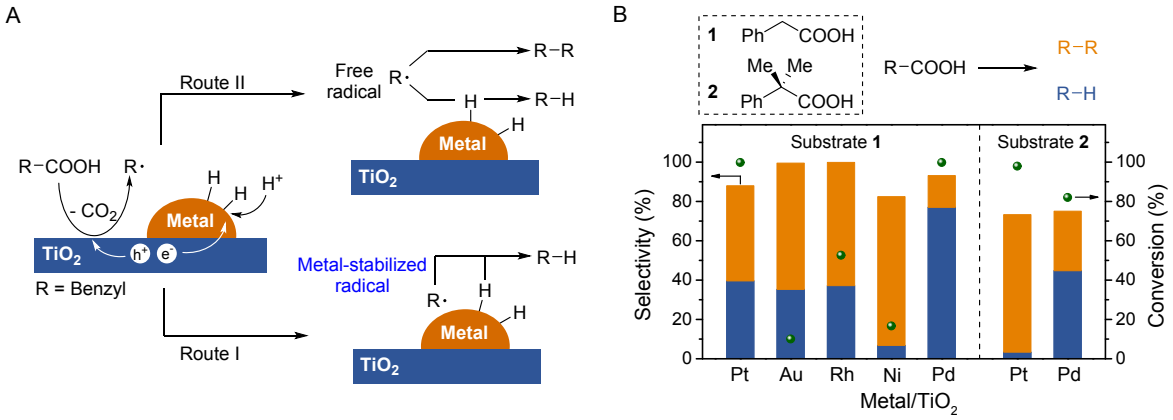

Figure 1. (**A**) Reaction network of phenylacetic acid conversion over metal/TiO_2 catalyst. (**B**) Photocatalytic conversion of phenylacetic acid and 2-phenylisobutyric acid over metal/TiO_2 catalysts. Reaction conditions: Substrate (0.15 mmol), photocatalyst (5 mg), acetonitrile (1.2 mL), Ar (0.1 MPa), room temperature (30 ± 5 °C), LEDs (365 nm, 18 W) irradiation for 3 h. Conversion and selectivity were determined by GC analysis.

Results and discussion

As a proof of concept, photocatalytic decarboxylation of phenylacetic acid **1** over metal/TiO_2 catalyst was chosen as model reaction. Phenylacetic acid **1** tends to dissociatively adsorb on TiO_2 surface, and under irradiation, photo-generated hole on TiO_2 can oxidize adsorbed carboxylate into an unstable carboxyl radical which would rapidly decompose into CO_2 and a free benzyl radical [26]. It is notable that oxidative decarboxylation of carboxylic acid is a convenient and effective protocol to deliver active radical intermediate, which has been widely applied in synthetic chemistry [27]. On the other hand, photo-generated electron would migrate to the metal deposits and reduce proton to form surface hydrogen species which would subsequently combine to release H_2. If the benzyl radical can be stabilized on metal catalyst center as we expect, it would preferentially combine with active hydrogen species on metal and deliver toluene as major product owing to the spatial proximity (Route I in Figure 1A). Otherwise, the radical intermediate would be free to diffuse and react randomly. It would

undergo homo-coupling to generate bibenzyl or react with the hydrogen species on metal to yield toluene, which eventually leads to a less selective product mixture (Route II in Figure 1A). Consequently, we can facilely deduce the interactions between metal and radical intermediate from the product distribution in the decarboxylation reaction over metal/TiO_2 catalysts. In addition, benzyl radical intermediate has strong and characteristic absorption bands in UV region, which makes it convenient to track the radical kinetics with *in situ* TA spectroscopy (vide infra).

A series of metal/TiO_2 catalysts (metal = Pt, Au, Rh, Ni, Pd) were prepared by an impregnation-calcination method, and used as the model catalysts to verify our hypothesis. Their powder XRD spectra indicate a characteristic pattern of mixed-phase TiO_2 (Degussa P25) (Figure S1). TEM images reveal that for Pt, Rh, Ni and Pd catalyst, the metal nanoparticles are dispersed on TiO_2 with a similar average size (1.6-1.8 nm) (Figure S2). However, metal aggregation is observed over Au/TiO_2 probably owing to the relatively weak interaction between Au and TiO_2. The size of Au nanoparticles is about 60-80 nm. In addition, CO-adsorption FT-IR study demonstrates that metal species dominantly exist in their metallic form for the synthesized catalysts (Figure S3, for detailed explanation, please refer to Supplement Note S1). As shown as in Figure 1B, the reaction of phenylacetic acid **1** is greatly influenced by the metal/TiO_2 catalyst employed. After irradiation for 3 h, the substrate was completely converted over Pt/TiO_2 and Pd/TiO_2 catalyst, and as predicted, benzyl radical was detected as the key intermediate during the reaction (Figure S4). In contrast, the conversion was rather low (< 20%) over Au/TiO_2 and Ni/TiO_2 catalyst. Such large gaps in conversion are expected to result from the distinct separation efficiencies of photo-generated carriers over different

catalysts. Photo-generated holes are the vital species to initiate the decarboxylation reaction. Meanwhile, Pd and Pt are the most effective metal co-catalysts to abstract electrons from excited TiO_2 and suppress the recombination process of photo-generated carriers [28]. Therefore, more holes are available to oxidize substrates on Pt/TiO_2 and Pd/TiO_2 catalyst, thus resulting in a remarkably faster conversion rate. In addition, other semiconductor photocatalysts with Pd deposition showed negligible activity for phenylacetic acid **1** activation (Figure S5), further demonstrating that TiO_2 is the active site to transform substrate into benzyl radical over metal/TiO_2 catalyst.

The subsequent conversion of benzyl radical determines product distribution. A similar product distribution was obtained over Pt/TiO_2, Au/TiO_2 and Rh/TiO_2, yielding bibenzyl as the major product (selectivity 48-64%) and toluene as the minor product (selectivity 35-40%) (Figure 1B). When Ni/TiO_2 was used as catalyst, the selectivity of toluene derived from the combination of radical intermediate and surface hydrogen species dropped to 7%, while bibenzyl was generated as the dominant product. This may be due to the intrinsic catalytic property of Ni as a similar result was reported in the electrocatalytic hydrogenation of benzaldehyde over different carbon-supported metal catalysts [29]. Compared to Pt, Rh and Pd, Ni delivered a markedly lower Faradaic efficiency toward aldehyde hydrogenation and instead, the hydrogen species on Ni would prefer to undergo H_2 evolution reaction. According to our proposed reaction patterns (Figure 1A), benzyl radical tends to react as a free radical over these four metal/TiO_2 catalysts, which is in accord with previous literatures [30-31]. However, a completely different product distribution was attained over Pd/TiO_2 catalyst. Toluene was obtained in a high yield (77%), whereas the production of bibenzyl from free

radical coupling only accounted for a minor proportion (16% yield), which implies a remarkably different reaction pattern for benzyl radical conversion over Pd/TiO_2 catalyst. We speculate that the benzyl radical generated on TiO_2 may adsorb and be stabilized on Pd nanoparticles which are rich in active hydrogen species as a result of continuous electron-induced proton reduction during the reaction. Therefore, it would preferentially go through a hydrogen termination process to produce toluene. This also can be demonstrated by the gaseous product analysis (Figure S6). Both Pt/TiO_2 and Pd/TiO_2 catalysts can achieve the full conversion of substrate after a reaction time of 3 h. However, compared to Pt/TiO_2, significantly lower amount of H_2 was generated over Pd/TiO_2, which indicates that electron-induced hydrogen species on Pd dominantly react with benzyl radicals instead of forming H_2. It is known that introduction of hydrogen on Pd would form relatively stable hydride (e.g., β-hydride) while not on the other four metals [32], so one may argue that the unexpectedly high selectivity for toluene production on Pd/TiO_2 arises from the higher accessibility of surface hydrogen species instead of the intimate interactions between radical intermediate and Pd. To verify this possibility, we changed the substrate to 2-phenylisobutyric acid **2**. Replacing phenylacetic acid **1** with **2** would not influence the proton reduction reaction to furnish surface hydrogen species, but offer a benzyl radical intermediate with large steric hindrance, which could impede its direct interaction with catalyst surface. When Pt/TiO_2 was used as catalyst, the production of cumene from radical intermediate hydrogenation was greatly suppressed as expected (Figure 1B), delivering a selectivity of 3%, ten times lower than that for toluene production from **1** conversion. The steric effect, however, was much less prominent for **2**

conversion over Pd/TiO_2 catalyst. The selectivity of hydrodecarboxylated product was 45%, just about 40% lower than

that for **1** conversion. This difference clearly illustrates that the interactions between metal and radical species play a more significant role for the preferential radical hydrogenation.

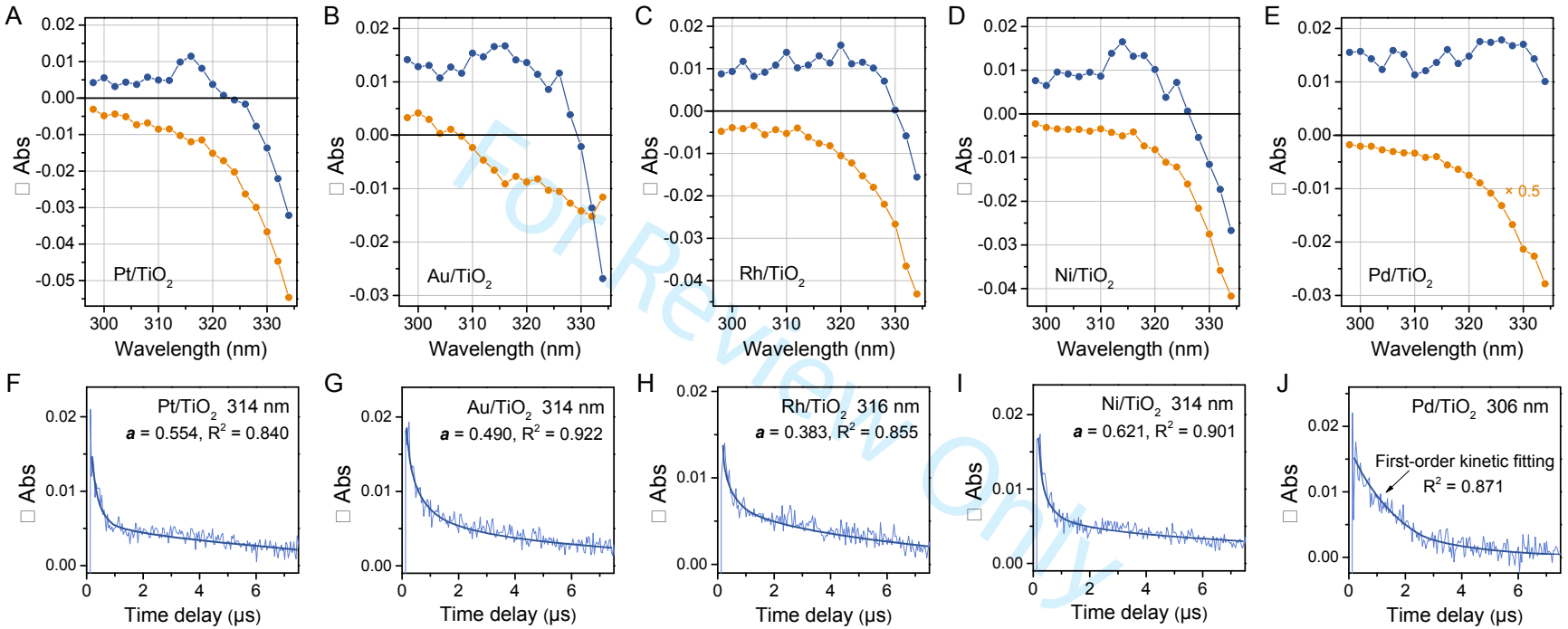

Figure 2. TA spectra averaged over 0.25-0.35 μs in the presence (blue) and absence (orange) of phenylacetic acid over (**A**) Pt/TiO_2, (**B**) Au/TiO_2, (**C**) Rh/TiO_2, (**D**) Ni/TiO_2, and (**E**) Pd/TiO_2 catalyst. Transient decay of benzyl radical absorption signal at selected wavelength over (**F**) Pt/TiO_2, (**G**) Au/TiO_2, (**H**) Rh/TiO_2, (**I**) Ni/TiO_2, and (**J**) Pd/TiO_2 catalyst. ***a***, the kinetic weight coefficient; R^2, the coefficient of fitting determination. Curves drawn on top of the data are guides to the eye.

Previously, researchers found that Pd/TiO_2 catalyst can promote the coupling reactions between aromatics and various radicals derived from hole-induced oxidation, and its outstanding performance was always attributed to the unique catalytic ability of Pd to activate aromatic moiety for the attack of radical species [33-34]. However, the direct interactions between metal deposits and radical species have been rarely explored. Radical species are known for their high reactivity. They generally possess a very short lifetime and exist in an extremely low concentration during the reactions, which renders them challenging to be detected and studied with conventional steady-state techniques [35].

In this study, we utilized TA spectroscopy to investigate the interactions between metal and photo-induced radical intermediate because of its unique ability to *in situ* track the evolution of transient species over nanosecond to microsecond timescales [36]. The tests were conducted in an acetonitrile solvent of phenylacetic acid **1** with catalyst suspension, and a laser pulse at 355 nm was used to excite TiO_2 to generate benzyl radical from substrate decarboxylation. A schematic representation of the TA system is shown in Figure S7. The averaged TA spectra recorded over 0.25-0.35 μs with different metal/TiO_2 catalysts are shown in Figure 2A-2E. In the absence of substrate **1**, negative bleaching signals are observed over these five metal/TiO_2 catalysts, and they grow stronger at longer wavelength, which is believed to derive from the intrinsic strong absorption of TiO_2 within this UV region [37]. When phenylacetic acid **1** was introduced, the TA patterns changed completely because the addition of **1** can continuously consume photo-generated carriers, and importantly, generate benzyl radicals that exhibit strong UV absorption bands. As shown in Figure 2A-2D, the TA spectra recorded over Pt/TiO_2, Au/TiO_2, Rh/TiO_2 and Ni/TiO_2 catalyst exhibit similar and

characteristic absorption bands at wavelengths below 330 nm with the absorption maximum at around 316 nm, which are analogous to those of free benzyl radicals derived from dibenzyl ketone/benzyl chloride photolysis [31, 38]. This absorption can be assigned to the $2^2A^2 \leftarrow X^2B^2$ transition of benzyl radical [25]. When Pd/TiO_2 is used as catalyst, the TA pattern remarkably changes and a broad absorption band over the whole detection range emerges (Figure 2E). In previous reports, the TA patterns of benzyl radicals varied with different substituent groups, structures and concentrations of radical precursor, and production methods [25, 38-39], indicating that the electronic states of generated radical are very sensitive to its local chemical environment. In our study, the testing conditions were almost identical except the metal species loaded on TiO_2. Therefore, we infer that the markedly broadened absorption band derives from the unique interactions between the supported Pd nanoparticles and benzyl radicals.

Furthermore, TA spectroscopy allows us to study the reaction kinetics of generated radical intermediate by directly monitoring the evolution of its characteristic adsorption bands. The transient decays of absorption signal at selected wavelength over different metal/TiO_2 catalysts are shown in Figure 2F-2J. A rapid decline in absorption intensity is observed at the early stage (< 1 μs) over Pt, Au, Rh and Ni catalyst, while the absorption signal decays in a slower and smoother manner over Pd catalyst, which implies that the conversion of benzyl radicals over Pd catalyst follows a reaction pathway distinct from those over the other four catalysts. Further analysis revealed a very interesting metal-dependent radical kinetics. According to the reaction network (Figure 1A), the radical intermediate generated from decarboxylation over excited TiO_2 can combine with hydrogen species on metal nanoparticles, or undergo homo-coupling to yield bibenzyl. The former pathway is a first-order reaction for benzyl radical conversion,

while the latter is a second-order route. Their reaction kinetics can be separately described as follows:

$$c_t = c_0 \exp(-k_1 t) \quad (1)$$

$$c_t = \frac{1}{k_2 t + {}^1/_{c_0}} \quad (2)$$

where c_0 and c_t correspond to the initial concentration of radical species and the concentration at a specific reaction time, respectively. k_1 and k_2 are the rate constants of the first-order and the second-order reaction mentioned above, respectively. Considering both reactions are possible pathways for benzyl radical conversion over metal/TiO_2 catalyst, we herein introduce a kinetic weight coefficient ($0 \leq \boldsymbol{a} \leq 1$) to evaluate the corresponding contribution from each pathway. Thereby the mixed reaction kinetics can be given as follows:

$$c_t = a c_0 \exp(-k_1 t) + \frac{1-a}{k_2 t + {}^1/_{c_0}} \quad (3)$$

The first and the second term on the right side of Equation 3 represent the relative contribution of hydrogen termination and homo-coupling pathway, respectively. According to the Lambert-Beer law ($\Delta\,\mathrm{Abs}_t = c_t \varepsilon l$, where ε is the molar attenuation coefficient and l is the optical path length), Equation 3 can be rearranged to

$$\Delta\,\mathrm{Abs}_t = a\,\Delta\,\mathrm{Abs}_0 \exp(-k_1 t) + \frac{1-a}{\frac{k_2}{\varepsilon l} t + {}^1/_{\Delta\,\mathrm{Abs}_0}} \quad (4)$$

A more detailed formula derivation and the corresponding illustration are displayed in Supplement Note S2. With Equation 4 in hand, we can directly deduce the reaction kinetics of benzyl radical conversion over metal/TiO_2 catalyst from the obtained transient decay.

The transient decay over Pt, Au, Rh and Ni catalyst can be fitted well to the mixed reaction kinetics (Equation 4) (Figure 2F-2I). The detailed fitting parameters are shown in Table S1. Notably, the kinetic weight coefficient (***a***) is 0.554, 0.490, 0.383, 0.621 for Pt, Au, Rh and Ni catalyst, respectively. These results indicate that both the combination with surface hydrogen species and radical homo-coupling are the major pathways for benzyl radical conversion. Although the contribution of each pathway slightly varies with different metal catalysts, probably owing to their distinct physicochemical properties, the unspecific reaction kinetics elucidates that radical species are prone to react in a free and uncontrolled manner over all these four metal/TiO_2 catalysts (Route II in Figure 1A). The transient decay over Pd/TiO_2 can be also fitted with Equation 4. Surprisingly, such fitting delivers a large ***a*** of 0.929 (Table S1), revealing a predominant pseudo-first-order kinetics for benzyl radical conversion, which has not been reported previously. Due to the minor contribution of the second-order pathway, the corresponding rate constant was obtained with a huge margin of error (Table S1, entry 5), implying that Equation 4 may be not suitable for the kinetic fitting over Pd catalyst. Alternatively, its TA signal evolution can be directly fitted with a simple monoexponential decay, that is, a first-order kinetic function (Figure 2J and Table S2). Similar first-order kinetic fitting is unsuitable for the other metal/TiO_2 catalysts as it leads to a markedly lower coefficient of fitting determination (R^2) (Table S2). In short, these transient kinetic analysis demonstrates that the radical conversion over Pd/TiO_2 catalyst follows a unique pseudo-first-order kinetics, which is remarkably different from that over other metal/TiO_2 catalysts. The interactions between Pd nanoparticles and benzyl radicals play an essential role in this process. It can be inferred that once the benzyl radicals are generated on TiO_2, Pd nanoparticles would efficiently

adsorb the free radicals and transform them into surface-stabilized species, thereby making their combination with surface hydrogen species as their dominant conversion pathway (Route I in Figure 1a). Such a conclusion from radical kinetics analysis is well consistent with the reaction results (Figure 1b). Consequently, with all these evidences, we can conclude that Pd nanoparticles are able to efficiently absorb extraneous active radicals and thus manipulate their subsequent conversion.

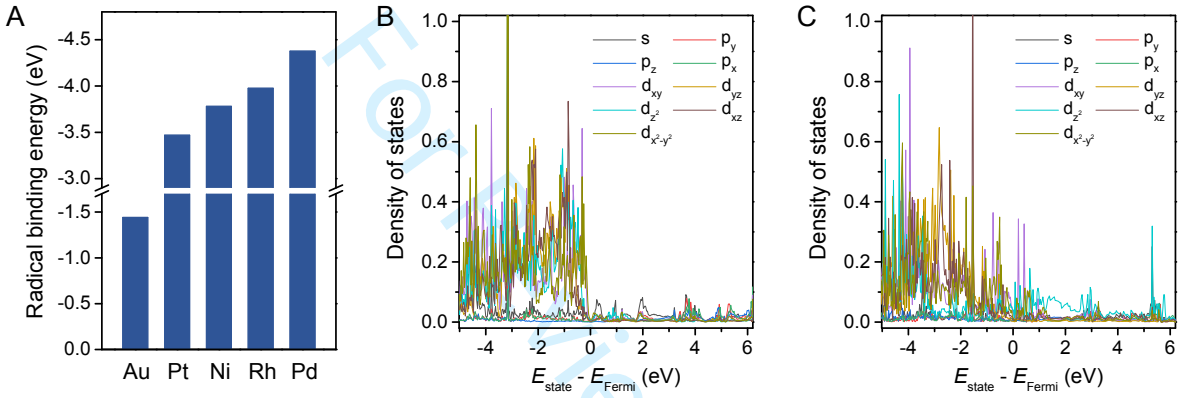

Figure 3. (**A**) The calculated binding energy of benzyl radical on different metal surfaces. The calculated partial density of states for benzyl radical binding on (**B**) Pd (111) and (**C**) Pt (111).

The unique catalytic activity of Pd urged us to explore in depth its interactions with radical species. Density functional theory (DFT) calculation revealed that the binding energy of benzyl radical on different metal surfaces increases in the sequence Au < Pt < Ni < Rh < Pd (Figure 3A). Therefore, the strong affinity for free radical is expected to be the prerequisite for controlling the conversion of extraneous radical species over Pd catalyst. Previously, Zhou et al. reported that compared to other metal species, supported Pd single atom catalyst exhibited markedly stronger binding ability of radical intermediates, thus leading to unselective mineralization of substrate [40], but the reason behind this phenomenon remained unexplored. By carefully analyzing the optimal adsorption conformations of benzyl radical on different

metal surfaces, we found that the radical binding energy follows an almost linear dependence on the bond distance between metal surface and benzyl carbon over noble metal catalysts (Au, Pt, Rh, and Pd) (Figure S8). The binding energy becomes obviously larger with shorter bond distance. It is known that the bond distance is in proportion to the degree of hybridization, that is, the integrated effect of electron donation from guest molecule (radical species herein) and back-donation from metal [41]. Here Pd delivers the shortest distance (2.132 Å), indicating its strong electronic interactions with radical species. Partial density of state (PDOS) analysis was further employed to provide deeper insights into the interactions between metal and benzyl radical. As shown in Figure 3B, upon radical binding on metal, the valence electrons of Pd dominantly concentrate in the electronic states with energy below the Fermi level. As a contrast, a more disperse distribution of electronic states is observed over Pt catalyst, and noticeable high-energy states with electron contribution from d_{xy} and d_{z^2} orbitals emerge (Figure 3C), which can be assigned to the electron population at antibonding π* and σ* orbitals, respectively. These evident differences are believed to arise from the distinct electronic structures of metal catalysts. Pd has a highly filled d-subshell ($4d^{10}$), which endows it with a strong ability to donate electrons and reallocate unpaired electrons from radical species, and hence contributes to forming a stable bonding, whereas Pt with more unfilled d orbitals allows the population of valence electrons at high-energy states upon electronic hybridization with extraneous radical species, thus destabilizing the generated bonding. Similarly, by analyzing the spin polarization, Gawargy et al. demonstrated that upon chemisorption on Pd, the unpaired spin of radical species is no longer concentrated in the organic moiety but drastically delocalized along the metal atoms [42]. These results together illustrate that the intrinsic

electronic structure of Pd and the resulting strengthened electronic interactions with radical species account for its strong affinity for free radical.

Scheme 1. The impact of reaction atmosphere for the conversion of phenylacetic acid over Pd/TiO_2 catalyst and substrate scope of hydrodecarboxylation reaction[a]

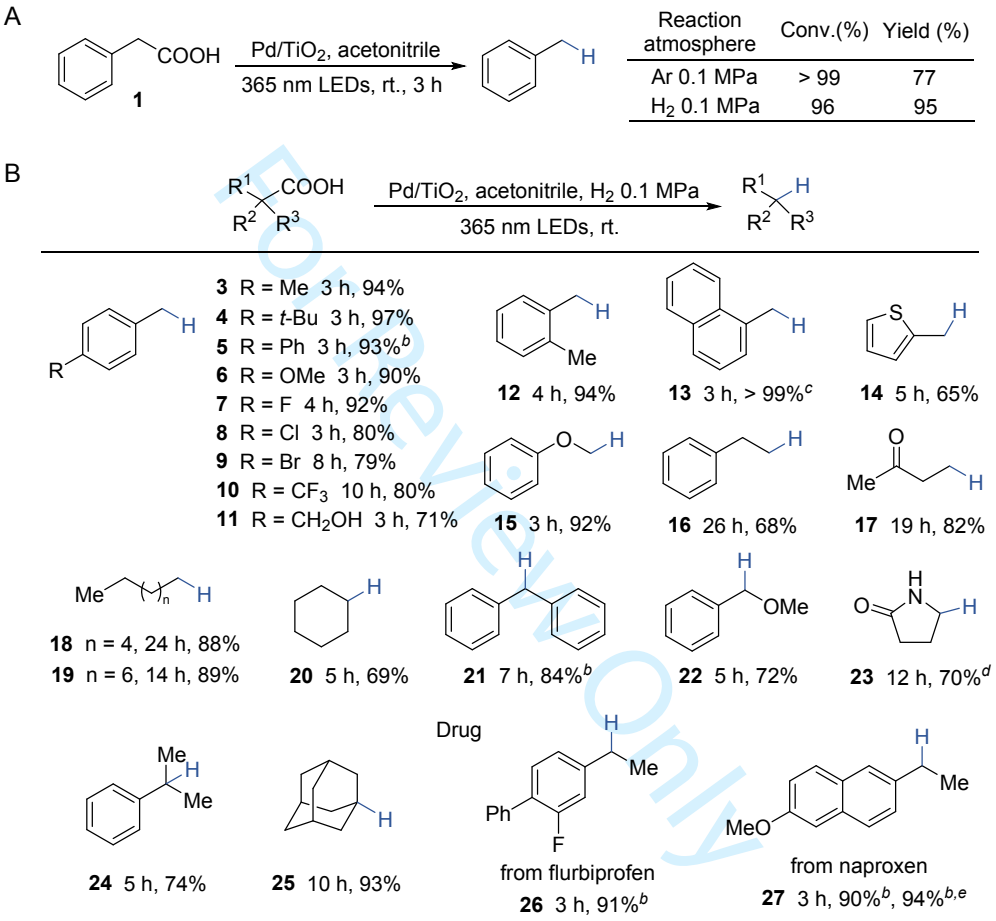

[a] GC yield. [b] Isolated yield. [c] NMR yield. [d] HPLC yield. [e] Reaction was carried out on a 3.75 mmol (0.863 g) scale, reaction time (18 h).

Moreover, subsequent transition state analysis revealed that the combination of benzyl radical and hydrogen species over Pd metal surface is a thermodynamically favorable process without any noticeable energy barriers (Figure S9). This suggests that the hydrogen termination of metal-stabilized radical intermediates is a very rapid and facile reaction despite the strong

binding energy of radical on Pd. Therefore, the strong metal-radical interaction on Pd would not hinder the subsequent conversion of radicals or poison the metal catalytic sites, but instead, endow the adsorbed radicals with new reactivity. In addition, given the critical role of metal electronic structure on the interactions with free radicals, alloying Pd with other metals to delicately tune the valence electron structure, for instance, would be a valid strategy for creating more efficient catalytic sites to regulate the conversion of extraneous radicals.

The interactions between metal catalyst and radical species provide great opportunities for the development of efficient heterogeneous catalytic systems. Since specific metal center, such as Pd, can stabilize extraneous free radicals on its surface, subtly tuning the local chemical environment or fabricating extra active catalytic sites on metal could efficiently transform the confined radical species into desired products. Herein, a proof-of-concept protocol for photocatalytic hydrodecarboxylation of carboxyl acids was developed over Pd/TiO_2 catalyst by boosting surface hydrogen concentration for the preferential hydrogenation of metal-stabilized radical intermediates. On one hand, Pd nanoparticles can rapidly trap the free radical intermediates derived from decarboxylation on TiO_2 and prevent them from reacting in an unregulated manner. On the other hand, in a H_2 atmosphere, H_2 can be facilely activated on Pd nanoparticles at room temperature (Figure S10) [43]. Therefore, the hydrogenation of radical species would be greatly enhanced. As shown in Scheme 1A, when changing the reaction atmosphere from Ar into H_2, the yield of toluene markedly increased from 77% to 95% for **1** conversion. By using our method, a wide range of carboxylic acids with various functional groups, including some drug molecules, can be successfully converted into the desired products in moderate to excellent yields (Scheme 1B). In addition, Pd/TiO_2 catalyst can be easily reused

without significant loss in activity (Figure S11). Hydrodecarboxylation is an important transformation in chemistry. Carboxylic group is one of the most frequently used directing groups for C–H bond activation and regioselective addition reactions [44-45], thereby effective hydrodecarboxylation enables it to be used as a traceless functional handle for the synthesis and post-modification of important organic structures [46]. In previous hydrodecarboxylation methods, pre-activation of substrate, elevated temperatures, extra base, and/or stoichiometric organic hydrogen donor were generally needed to initiate the reaction and regulate the conversion of radical intermediates [47-49], whereas they are no longer required in our system owing to the integration of the strong photoredox ability of TiO_2 and the unique catalytic activity of Pd. Especially, the latter, the ability of Pd to interact with extraneous free radicals, is of fundamental importance for the controllable radical reaction. More studies devoted to selective radical conversion over heterogeneous catalyst are on going in our laboratory.

Conclusions

In this article, we demonstrated the feasibility of utilizing metal-radical interaction to manipulate the conversion of extraneous free radicals with a combination of experimental, spectral, and theoretical methods. Among a series of metal/TiO_2 catalysts, Pd/TiO_2 exhibited unexpectedly high selectivity for the hydrogen termination of benzyl radicals generated from TiO_2. Meanwhile, *in situ* TA study indicated a predominant pseudo-first-order kinetics for benzyl radical conversion over Pd/TiO_2, completely distinct from the common free radical pathway. These results clearly illustrate that Pd nanoparticles are capable of efficiently capturing extraneous benzyl radicals onto the metal surface, thereby regulating their subsequent conversion in a controllable manner. Further theoretical calculation reveals that the

enhanced electronic interactions between metal and radical species account for the strong affinity for free radical over Pd catalyst. Subtly regulating the local microenvironment on metal could drive surface-stabilized radical species to undergo the desired downstream reactions. Following this design concept, an effective protocol for hydrodecarboxylation of various carboxylic acids was successfully developed by increasing surface hydrogen concentration for the preferential hydrogenation of metal-stabilized radical species. Fabricating catalytic sites, such as the suitable metal catalyst, to timely trap the transient active intermediates and prevent them from reacting in an unregulated manner, is always the essential prerequisite for a controllable reaction pattern. The understandings about metal-radical interaction demonstrated here are applicable for other important radical-mediated processes beyond photocatalysis.

Conflict of interest

The authors declare no conflict of interest.

Acknowledgement

The authors are grateful for the financial support of the Ministry of Science and Technology of the People's Republic of China (2018YFE0118100), the National Natural Science Foundation of China (22025206, 21721004, 21991090, 22002159, 22088102, 21833009), the Liaoning Revitalization Talents Prograrn (XLYC2002012, XLYC1802126), the Joint Fund of the Yulin University and the Dalian National Laboratory for Clean Energy (Grant.YLU-DNL Fund 2021019), the Scientific Instrument Developing Project of the Chinese Academy of Sciences (YJKYYQ20190003), Dalian Science and Technology Innovation Fund (2019J12GX031), and Dalian Institute of Chemical Physics, Chinese Academy of Sciences (DICP I202009). The authors also thank the instrumental support of the Fundamental Research

Center of Artificial Photosynthesis (FReCAP) and the Liaoning Key Laboratory of Biomass Conversion for Energy and Material. The authors would like to dedicate this paper to Prof. Ke-Li Han, who unfortunately passed away in March 2022.

References

[1] J. Xie, H. Jin, A. S. K. Hashmi, *Chem. Soc. Rev.*, **2017**, 46, 5193-5203.

[2] P. Sivaguru, Z. Wang, G. Zanoni, X. Bi, *Chem. Soc. Rev.*, **2019**, 48, 2615-2656.

[3] Z. Huang, N. Luo, C. Zhang, F. Wang, *Nat. Rev. Chem.*, **2022**, 6, 197-214.

[4] F. Recupero, C. Punta, *Chem. Rev.*, **2007**, 107, 3800-3842.

[5] D. Staveness, I. Bosque, C. R. J. Stephenson, *Acc. Chem. Res.*, **2016**, 49, 2295-2306.

[6] H. Kisch, *Angew. Chem., Int. Ed.*, **2013**, 52, 812-847.

[7] K. L. Skubi, T. R. Blum, T. P. Yoon, *Chem. Rev.*, **2016**, 116, 10035-10074.

[8] A. Y. Chan, I. B. Perry, N. B. Bissonnette, B. F. Buksh, G. A. Edwards, L. I. Frye, O. L. Garry, M. N. Lavagnino, B. X. Li, Y. Liang, E. Mao, A. Millet, J. V. Oakley, N. L. Reed, H. A. Sakai, C. P. Seath, D. W. C. MacMillan, *Chem. Rev.*, **2022**, 122, 1485-1542.

[9] A. Hainer, N. Marina, S. Rincon, P. Costa, A. E. Lanterna, J. C. Scaiano, *J. Am. Chem. Soc.*, **2019**, 141, 4531-4535.

[10] H. Kisch, *Acc. Chem. Res.*, **2017**, 50, 1002-1010.

[11] F. J. Holzhäuser, J. B. Mensah, R. Palkovits, *Green Chem.*, **2020**, 22, 286-301.

[12] D. W. Manley, R. T. McBurney, P. Miller, R. F. Howe, S. Rhydderch, J. C. Walton, *J. Am. Chem. Soc.*, **2012**, 134, 13580-13583.

[13] D. W. Manley, J. C. Walton, *Org. Lett.*, **2014**, 16, 5394-5397.

[14] D. Ma, A. Liu, S. Li, C. Lu, C. Chen, *Catal. Sci. Technol.*, **2018**, 8, 2030-2045.

[15] Q. Zhu, D. G. Nocera, *J. Am. Chem. Soc.*, **2020**, 142, 17913-17918.

[16] D. Kuwana, Y. Komori, M. Nagatomo, M. Inoue, *J. Org. Chem.*, **2022**, 87, 730-736.

[17] B. E. Bent, *Chem. Rev.*, **1996**, 96, 1361-1390.

[18] Z. Ma, F. Zaera, *Surf. Sci. Rep.*, **2006**, 61, 229-281.

[19] J. Lee, D. B. Dougherty, J. T. Yates, Jr., *J. Am. Chem. Soc.*, **2006**, 128, 6008-6009.

[20] J. Anibal, A. Malkani, B. Xu, *Catal. Sci. Technol.*, **2020**, 10, 3181-3194.

[21] Y. Li, P. Ren, D. Zhang, W. Qiao, D. Wang, X. Yang, X. Wen, M. H. Rummeli, H. Niemantsverdriet, J. P. Lewis, F. Besenbacher, H. Xiang, Y. Li, R. Su, *ACS Catal.*, **2021**, 11, 4338-4348.

[22] R. Bar-Ziv, I. Zilbermann, O. Oster-Golberg, T. Zidki, G. Yardeni, H. Cohen, D. Meyerstein, *Chem. Eur. J.*, **2012**, 18, 4699-4705.

[23] R. Bar-Ziv, I. Zilbermann, M. Shandalov, V. Shevchenko, D. Meyerstein, *Chem. Eur. J.*, **2015**, 21, 19000-19009.

[24] Z. Zhang, A. Berg, H. Levanon, R. W. Fessenden, D. Meisel, *J. Am. Chem. Soc.*, **2003**, 125, 7959-7963.

[25] R. F. C. Clarldge, H. Fischer, *J. Phys. Chem.*, **1983**, 87, 1960-1967.

[26] H. Zhang, P. Zhou, H. Ji, W. Ma, C. Chen, J. Zhao, *Appl. Catal., B*, **2018**, 224, 376-382.

[27] J. Schwarz, B. König, *Green Chem.*, **2018**, 20, 323-361.

[28] K. Shimura, H. Yoshida, *Energy Environ. Sci.*, **2011**, 4, 2467-2481.

[29] Y. Song, U. Sanyal, D. Pangotra, J. D. Holladay, D. M. Camaioni, O. Y. Gutiérrez, J. A. Lercher, *J. Catal.*, **2018**, 359, 68-75.

[30] A. L. J. Beckwith, V. W. Bowry, K. U. Ingold, *J. Am. Chem. Soc.*, **1992**, 114, 4983-4992.

[31] E. C. Korolenko, F. L. Cozens, J. C. Scaiano, *J. Phys. Chem.*, **1995**, 99, 14123-14128.

[32] H. Kobayashi, H. Morita, M. Yamauchi, R. Ikeda, H. Kitagawa, Y. Kubota, K. Kato, M. Takata, *J. Am. Chem. Soc.*, **2011**, 133, 11034-11037.

[33] E. Wada, T. Takeuchi, Y. Fujimura, A. Tyagi, T. Kato, H. Yoshida, *Catal. Sci. Technol.*, **2017**, 7, 2457-2466.

[34] A. Tyagi, T. Matsumoto, A. Yamamoto, T. Kato, H. Yoshida, *Catal. Lett.*, **2020**, 150, 31-38.

[35] L. Lewis-Borrell, M. Sneha, A. Bhattacherjee, I. P. Clark, A. J. Orr-Ewing, *Chem. Sci.*, **2020**, 11, 4475-4481.

[36] Y. Yang, J.-S. Chen, J.-Y. Liu, G.-J. Zhao, L. Liu, K.-L. Han, T. R. Cook, P. J. Stang, *J. Phys. Chem. Lett.*, **2015**, 6, 1942-1947.

[37] Á. Morales-García, R. Valero, F. Illas, *J. Phys. Chem. C*, **2020**, 124, 11819-11824.

[38] N. A. McAskill, D. F. Sangster, *Aust. J. Chem.*, **1977**, 30, 2107-2113.

[39] T. Izumida, T. Ichikawa, H. Yoshlda, *J. Phys. Chem.*, **1980**, 84, 60-63.

[40] P. Zhou, Y. Chao, F. Lv, K. Wang, W. Zhang, J. Zhou, H. Chen, L. Wang, Y. Li, Q. Zhang, L. Gu, S. Guo, *ACS Catal.*, **2020**, 10, 9109-9114.

[41] M. De Santis, S. Rampino, L. Storchi, L. Belpassi, F. Tarantelli, *Inorg. Chem.*, **2019**, 58, 11716-11729.

[42] T. A. Gawargy, P. Costa, A. E. Lanterna, J. C. Scaiano, *Org. Biomol. Chem.*, **2020**, 18, 6047-6052.

[43] Z. Huang, Z. Zhao, C. Zhang, J. Lu, H. Liu, N. Luo, J. Zhang, F. Wang, *Nat. Catal.*, **2020**, 3, 170-178.

[44] H. B. Kagan, O. Riant, *Chem. Rev.*, **1992**, 92, 1007-1019.

[45] J. He, M. Wasa, K. S. L. Chan, Q. Shao, J.-Q. Yu, *Chem. Rev.*, **2017**, 117, 8754-8786.

[46] J. D. Griffin, M. A. Zeller, D. A. Nicewicz, *J. Am. Chem. Soc.*, **2015**, 137, 11340-8.

[47] Y. Yoshimi, T. Itou, M. Hatanaka, *Chem. Commun.*, **2007**, 5244-5246.

[48] E. J. Ko, G. P. Savage, C. M. Williams, J. Tsanaktsidis, *Org. Lett.*, **2011**, 13, 1944-1947.

[49] T. Qin, L. R. Malins, J. T. Edwards, R. R. Merchant, A. J. Novak, J. Z. Zhong, R. B. Mills, M. Yan, C. Yuan, M. D. Eastgate, P. S. Baran, *Angew. Chem., Int. Ed.*, **2017**, 56, 260-265.

GRAPHICAL ABSTRACT

Controlling the Reactions of Free Radicals with Metal-Radical Interaction

Zhipeng Huang,† Yang Yang,† Junju Mu, Genheng Li, Jianyu Han, Puning Ren, Jian Zhang, Nengchao Luo, Ke-Li Han, Feng Wang*

Dalian Institute of Chemical Physics, Chinese Academy of Sciences, Dalian 116023, China

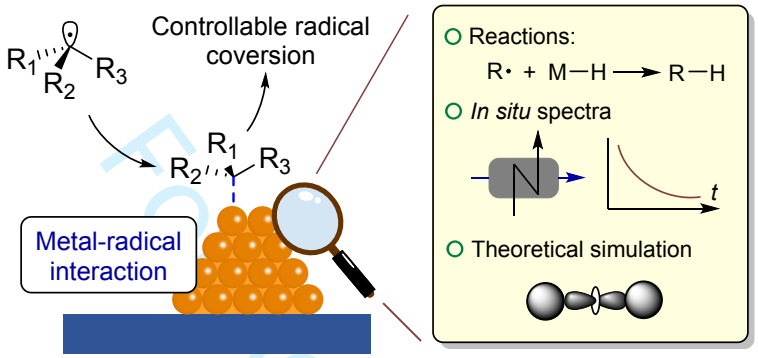

Supported Pd nanoparticles can stabilize extraneous free radicals and manipulate their subsequent conversion via the strong metal-radical interaction, which has been detailedly elucidated by photocatalytic reactions, *in situ* transient absorption spectroscopy, and theoretical simulation.

Supplementary Material for

Controlling the Reactions of Free Radicals with Metal-Radical Interaction

Zhipeng Huang,[1,2,†] Yang Yang,[3,†] Junju Mu,[1] Genheng Li,[1,4] Jianyu Han,[1,2] Puning Ren,[1,2] Jian Zhang,[1] Nengchao Luo,[1] Ke-Li Han,[3] Feng Wang[1,*]

[1] State Key Laboratory of Catalysis, Dalian National Laboratory for Clean Energy, Dalian Institute of Chemical Physics, Chinese Academy of Sciences, Dalian 116023, China

[2] University of Chinese Academy of Sciences, Beijing 100049, China

[3] State Key Laboratory of Molecular Reaction Dynamics, Dalian Institute of Chemical Physics, Chinese Academy of Sciences, Dalian 116023, China

[4] Zhang Dayu School of Chemistry, Dalian University of Technology, Dalian 116024, China

[†] These authors contributed equally to this work.

*Corresponding author. E-mail: wangfeng@dicp.ac.cn

Materials and reagents

All chemicals are of analytical grade and used as purchased without further purification. Phenylacetic acid (> 98%) was purchased from Sinopharm Chemical Reagent. 4-Methylphenylacetic acid (98%), (4-*tert*-butylphenyl)acetic acid (98%), 4-biphenylacetic acid (98%), 4-methoxyphenylacetic acid (98%), 4-fluorophenylacetic acid (98%), 4-chiorophenylacetic acid (98%), 4-bromophenylacetic acid (98%), 4-(hydroxymethyl)phenylacetic acid (97%), 2-methylphenylacetic acid (99%), DL-*α*-methoxyphenylacetic acid (98%), 2-thiopheneacetic acid (98%), phenoxyacetic acid (98%), octanoic acid (98%), and 4-(trifluoromethyl)phenylacetic acid (99%) were purchased from Energy Reagent. 2,2-Diphenylacetic acid (99.9%) was purchased from Bidepharmate Reagent. 2-Phenylisobutyric acid (97%), 1-adamantanecarboxylic acid (98%), and naproxen (98%) were purchased from Macklin Reagent. 1-Naphthylacetic acid (96%), 3-phenylpropionic acid (> 99%), decanoic acid (99%), laevulinic acid (99%), cyelohexanecarboxylic acid (99%), L-pyroglutamic acid (99%), flurbiprofen (99%), and 2,2,6,6-tetramethylpiperidinooxy (TEMPO) were purchased from Aladdin Reagent. Reaction solvents were purchased from Sinopharm Chemical Reagent. Noble metal salts were purchased from the Non Ferrous Metal Institute of Shenyang.

Catalyst preparation

The Pd/TiO_2 catalyst was synthesized by an impregnation-calcination method. Typically, 0.5 g of TiO_2 (Degussa P25) was added into a 20 mL aqueous solution of $PdCl_2$ containing 5 mg of Pd. The slurry was stirred at room temperature for 12 h, and then the solvent was evaporated at 105 °C. The obtained powder was firstly calcined in air flow (30 mL min^{-1}) at 400 °C for 2 h. When cooled to room temperature, the calcined sample was further reduced in H_2 flow (30 mL min^{-1}) at 350 °C for 2 h. The ramping rate of both procedures was 10 °C min^{-1}. Other metal/TiO_2 catalysts, including Pt/TiO_2, Au/TiO_2, Ni/TiO_2, and Rh/TiO_2, were prepared via a similar procedure except using H_2PtCl_6, $HAuCl_4$, $NiCl_2 \cdot 6H_2O$, and $RhCl_3$ as metal precursors, respectively. Pd/CeO_2 was also prepared via a similar procedure except different support used. Pd/In_2O_3, Pd/CdS, and Pd/g-C_3N_4, were synthesized via a

photodeposition method. CeO_2, In_2O_3, CdS were prepared according to literatures [1-3]. g-C_3N_4 was prepared by heating melamine at 550 °C for 4 h. Without specific statement, the content of metal deposition in all mentioned catalysts was 1 wt% relative to the supports.

General characterization

X-ray diffraction (XRD) analysis was conducted on a PANAlytical X'Pert PRO-1 diffractometer, using Cu-Kα radiation at 40 kV and 20 mA. The data were recorded over a 2θ range of 10-90°.

The transmission electron microscopy (TEM) images of Pd/TiO_2 were obtained on a JEOL JEM-ARM200F field emission transmission electron microscope equipped with high angle annular dark field (HAADF) detectors at an accelerating voltage of 200 kV. The TEM images of Pt/TiO_2, Ni/TiO_2, Rh/TiO_2 and Au/TiO_2 were obtained on JEOL JEM-2100 field emission transmission electron microscope at an accelerating voltage of 200 kV. The calculation of size distribution of metal nanoparticle was based on more than 120 particles in the TEM images. The X-ray energy dispersive (EDX) spectrum was obtained by JEM-2100 energy dispersive spectrometer.

CO adsorption Fourier transform-infrared (FT-IR) spectra were collected on a Bruker Tensor 27 instrument. The catalyst sample (~ 30 mg) were pressed into a self-supporting disk (13 mm in diameter), and then placed into a homemade IR quartz cell attached to a closed glass-circulation system. And then the quart cell was vacuumed and the sample was simultaneously heated to 150 °C for 30 min. When the pre-treated sample was cooled to 25 °C, background spectra was collected. Subsequently, highly pure CO was injected from a gas cylinder. Finally, the spectra were recorded after the system had been vacuumed for 1-2 min to remove the physically absorbed CO. For Au/TiO_2 and Ni/TiO_2 which have a relatively weak binding energy of CO, the physically absorbed CO was removed by Ar purging instead of vacuum treatment.

Temperature-programmed desorption (TPD) experiments were conducted in a U-type quart tube connected to a mass spectrometer (GSD320 Thermostar). Typically, 500 mg of catalyst sample was placed in a U-type quart tube, heated to 450 °C and kept for 60 min in Ar

flow (30 mL min^{-1}). When the sample was cooled down to 25 °C, the flow was switched to H_2 (20 mL min^{-1}) for 40 min, followed by purging with Ar (20 mL min^{-1}) for 30 min to remove unreacted H_2. And then the sample was heated to 450 °C with a ramping rate of 10 °C min^{-1} in Ar flow, and the TPD profiles were recorded, simultaneously.

Transient absorption (TA) spectral investigation

TA study was conducted in a home-made Laser Flash photolysis (LFP) system equipped with a nanosecond transient absorption and emission spectroscopy (NTAS) [4-5]. The whole experiment setup is made of four parts:

(1) The excitation source is a Nd:YAG nanosecond laser system (Nimma900, Beamtech Optronics Co., Ltd.) with the third-harmonic output of Max270 mJ pulse energy@355 nm laser wavelength@8ns pulse duration, operating at a repetition rate of 3 Hz. The laser beam had a diameter of about 10 mm and irradiated the sample without being focused.

(2) The monitoring system consists of a pulsed 450 W xenon lamp as the probe light, a monochromator (WDG30-Z, Beijing Optical Instrument Factory), a photomultiplier tube (PMT, CR131, Hamamatru, with detection wavelength range from 200 nm to 900 nm) at the detection end. The transient curve is recorded by digital oscilloscope (Tektronix, MDO3052, analog channel bandwidth 500 M, sampling rate up to 2.5 G s^{-1}). Full width at half maximum (FWHM) of apparatus response function is 25 ns. After passing through double focal lens, the monitoring light had a beam diameter of 2 mm, and then irradiated the excited sample with its propagating direction perpendicular to that of the excitation beam.

(3) The timing sequence of all the component parts is realized via the pulse generator (PG801, Dalian Institute of Chemical Physics) with the system jitter below 1 ns.

(4) A labview computer program based on graphic user interface was written to control the experiments, gather the data, process information and produce suitable data files on storage devices.

TA spectroscopy herein was used to investigate the generation and reaction kinetics of

benzyl radical over heterogeneous catalysts (metal/TiO_2), which has been rarely reported in previous studies. A magnetic stirrer was used to keep the catalyst in suspension during TA tests. In addition, benzyl radical has characteristic absorption bands at 300-330 nm. However, the second-order grating diffraction light and laser-induced fluorescence from TiO_2 dramatically interfere the detection and subsequent analysis of benzyl radical. Therefore, two shortpass filters with transmittance at 250-530 nm and bandstop at 575-665 nm were utilized to minimize their influence. Moreover, the generation of benzyl radical in our system is a secondary process from laser stimulation. That is, laser firstly excites the TiO_2-based catalyst, and then photo-generated hole from TiO_2 oxidizes substrate to generate benzyl radical, indicating a low production efficiency. Thereby, a delicately designed sample cell with an extended optical path (30 mm) was used (Figure S7). In principle, the higher laser intensity is employed, the more benzyl radicals could be generated. However, under strong laser irradiation, electrons accumulated on TiO_2 would reduce Ti^{4+} to form long-lived Ti^{3+} centers which exhibit strong TA in UV region [6], thus interfering the observation of benzyl radical. Therefore, the laser intensity was optimized. The laser intensity was 10.0-11.6 mJ cm^{-2}. The tests were conducted in an acetonitrile solvent of phenylacetic acid (20 mmol L^{-1}) with catalyst suspension (0.175 mg mL^{-1}). The sample solution was deaerated through nitrogen bubbling for 40 min before testing. A short-time ultrasonic treatment is helpful to disperse solid catalyst into solution. Each spectrum was the average result of multiple measurements (10 times for TA spectra at 298-334 nm, and 100 times for kinetics decay at selected wavelength).

General procedure for photocatalytic reaction

The photocatalytic reactions were conducted in the home-made LEDs photoreactors [7]. Typically, the substrate (0.15 mmol), solvent (1.2 mL) and catalyst (5 mg) were added into a quartz tube with a magnetic bar. The inner atmosphere was repeatedly evacuated by a water pump and recharged with Ar (0.1 MPa) for 5 times. For the reactions conducted in a H_2 atmosphere, the inner atmosphere was further repeatedly evacuated and recharged with H_2 (0.1 MPa) for 5 times. The reaction solvent was stirred for 10 min, and then irradiated with LEDs (18 W, 365 nm) with continuous stirring at ambient temperature (30 ± 5 °C). The stirring rate

was 550-600 rpm. For the cyclic experiment, after reaction the catalyst was separated by centrifugation, and filtrate was used for further analysis. The catalyst was washed with anhydrous ethanol for 4 times and dried overnight in vacuum at 40 °C. Then the catalyst can be used directly for the next run.

The scale-up reaction of naproxen was conducted in an autoclave photoreactor with a window on top. The substrate (3.75 mmol), acetonitrile (30 mL) and Pd/TiO_2 catalyst (125 mg) were added into the internal Teflon insert. The reactor was sealed, and the inner atmosphere was repeatedly changed with Ar (0.5 MPa) and finally charged with H_2 (0.1 MPa). Subsequently, the reactor was irradiated with LEDs (105 W, 365 nm). The temperature maintained 35-40 °C during the reaction. After reaction, the product was separated by preparative thin-layer chromatography (TLC).

Product analysis

The products were identified by a gas chromatography-mass spectrometry (GC-MS, Agilent 7890A/5975C) with a HP-5 column, and quantitatively analyzed by GC or high-performance liquid chromatography (HPLC, Agilent). For the reaction of substrates with a relative low boiling point, the analysis was carried out in a GC (Agilent, 7890B) with a DB-FFAP column. After reaction, 4-methylanisole was added to the reaction solvent as the internal standard. Then the mixture was filtered through a 0.22 μm Nylon syringe filter and the filtrate was then quantified with GC. GC conditions: Injector temperature, 260 °C; carrier gas, highly pure N_2; temperature program, initial temperature 50 °C, then increasing by 10 °C min^{-1} to 220 °C, finally maintained 220 °C for 2 min; detection temperature 260 °C. For the reaction of substrates with a high boiling point, the products were analyzed by GC (Agilent, 7890A) with a HP-5 column and a derivatization procedure was needed prior to analysis [8]. Typically, after reaction, 4-methylanisole (as the internal standard), N,O-bis(trimethylsiyl)trifluoroacetamide (BSTFA) and trimethylchlorosilane (TSCS) mixture (99:1, 100 μL) and pyridine (200 μL) were added to the reaction mixture. The mixture was heated in an oil bath (60 °C) for 60 min. Subsequently, the solvent was analyzed with GC after filtration with a Nylon syringe filter. GC conditions: Injector temperature, 260 °C; carrier gas, highly pure N_2; temperature program,

first maintaining 100 °C for 2 min, then increasing by 10 °C min^{-1} to 280 °C, finally maintained 280 °C for 2 min; detection temperature, 280 °C. For the reaction of L-pyroglutamic acid, the quantitative analysis was conducted in HPLC with a PFP column because of the unpromising resolution of this substrate and its product in GC. Anisole was used as the internal standard and added to the reaction solvent after reaction. Then the mixture was filtered through a Nylon syringe filter and diluted with ethanol. Finally, the obtained solvent was quantified with HPLC. HPLC conditions: Injection, 5 μL; mobile phase, acetonitrile/H_2O mixture with a minor amount of phosphoric acid solvent (1 mol L^{-1}); TCC temperature, 35 °C; detector, UV 254 nm. The quantitative analysis of 1-methylnaphthalene produced from 1-naphthylacetic acid was carried out with ^1H NMR because pure 1-methylnaphthalene is not commercially available, thus impeding its accurate quantitation with GC or HPLC. In this case, mesitylene was used as the internal standard. All abovementioned quantitative results from GC, HPLC and NMR were repeated at least twice in order to guarantee the accuracy of data. The isolated yields were obtained by preparative thin-layer chromatography (TLC).

The conversion was calculated as mole percentage as followed:

$$\text{Conversion (mol \%)} = \left(1 - \frac{\text{n(Feedstock after reaction)}}{\text{n(Feedstock before reaction)}}\right) \times 100\% \quad \text{(S1)}$$

The yield of hydrodecarboxylated product was calculated as mole percentage as followed:

$$\text{Yield (mol \%)} = \frac{\text{n(Product)}}{\text{n(Feedstock before reaction)}} \times 100\% \quad \text{(S2)}$$

The yield of product derived from radical C–C coupling was calculated as mole percentage as followed:

$$\text{Yield (mol \%)} = \frac{\text{n(Product)}}{\text{n(Feedstock before reaction)}} \times 2 \times 100\% \quad \text{(S3)}$$

Gaseous products were detected by a GC (Shimadzu, GC-2014) equipped with thermal conductivity detector (TCD) and a TDX-01 column. The quantified analysis of CO_2 was conducted on the same GC with CH_4 as the internal standard. The quantified analysis of H_2 was conducted on a Techcomp 7900 GC quipped with TCD and a TDX-01 column. He was used as the internal standard.

Density functional theory (DFT) calculation

Spin-polarized DFT calculations were performed using the Vienna Ab Initio Package (VASP) [9-10], where the ionic cores were described by the projected augmented wave (PAW) pseudopotentials [11-12] and valence electrons were explicitly considered using a plane-wave basis set with energy cutoffs of 400 eV throughout the study. The generalized gradient approximation (GGA) using the PBE functional were applied [13], and Grimme's DFT-D3 methodology was used to describe the dispersion interactions among all the atoms [14].

The primitive cells of bulk face-centered Au, Pt, Ni, Rh and Pd were first optimized where the Brillouin zone was sampled using 9 × 9 × 9 Γ-centered Monkhorst−Pack grid meshes. The slabs with (111) facet surface were constructed using the optimized primitive cells of the Au, Pt, Ni, Rh and Pd systems. These surfaces were chosen as simulated models because of their thermal stability [15]. Each slab was created with four metal layers, with each layer consisting of 16 atoms. The metal layers were separated by a vacuum layer of 15 Å to mitigate the interaction between the slab and its periodic replicas. In all calculations related to the slabs, the bottom two metal layers were fixed to their bulk configurations, while the top two metal layers and the adsorbates were free to relax in all directions. Brillouin zone integration was performed using 3 × 3 × 1 Γ-centered Monkhorst−Pack grid meshes and Gaussian smearing of 0.1 eV. All self-consistent field (SCF) calculations were converged to 1×10^{-5} kJ mol^{-1}. All atomic coordinates of the adsorbates and the metal atoms in the top two layers were optimized to a force of less than 0.02 eV Å^{-1} on each atom. The projected density of state (PDOS) of the optimized geometries were calculated using the HSE06 exchange-correlation function implemented [16].

The adsorption energies of all the gas-phase-stable surface intermediates reported in this paper were calculated in their most favorable adsorption modes. The adsorption energies, E_{ads}, were calculated as follow:

$$E_{ads} = E_{ads+adsorbate} - E_{ads} - E_{adsorbate(gas)} \quad (S4)$$

where $E_{slab+adsorbate}$ is the total energy of the slab with an adsorbate binding onto it, E_{slab} is the total energy of the clean metal slab, and $E_{adsorbate(gas)}$ is the total energy of the adsorbate in the gas phase.

The transition state of each elementary reaction step was located by the Climbing Image Nudged Elastic Band (CI-NEB) [17], where the path between the reactant(s) and product(s)

was discretized into a series of four structural images. After the CI-NEB calculation, the image that corresponds to the saddle point in the free energy surface was regarded as the transition state structure.

Supplementary notes

Note S1. CO-absorption FT-IR study

CO-absorption FT-IR spectroscopy was employed to investigate the chemical states of metal species on metal/TiO_2 catalysts. In the FT-IR spectra of Pt/TiO_2 (Figure S3A), the bands at 2077 and 1831 cm^{-1} can be assigned to the vibrations of linear and bridge-bonded CO adsorbed on metallic platinum crystals, respectively [18]. In Figure S3B, the bands at 2094 and 2027 cm^{-1} can be assigned to the gem-dicarbonyl species on reduced Rh clusters [19]. Similarly, in the FT-IR spectra of Pd/TiO_2 (Figure S3C), the band at 2084 cm^{-1} can be assigned to the CO linearly adsorbed on metallic palladium, and the broad band around 1937 cm^{-1} derives from the vibrations of multi-bonded CO [20]. Due to the relatively weak binding of CO on Au and Ni, the physically absorbed CO was removed by Ar purging instead of vacuum treatment when collecting the spectra of Au/TiO_2 and Ni/TiO_2. Therefore, we can observe the band of weakly absorbed CO on the surface cations, Ti^{4+} (2171 cm^{-1}) (Figure S3D and S3E). In Figure S3D, the band at 2119 cm^{-1} illustrates the adsorption of CO on metallic gold particles [21]. In the FT-IR spectra of Ni/TiO_2 (Figure S3E), a band at around 2119 cm^{-1} is observed, which can be assigned to carbonyl complexes of Ni^+ on reduced nickel sites [22]. The Ni^+ ions are formed via a back π-bond interaction with CO. In short, these FT-IR studies demonstrate that the metal species dominantly exist in their metallic form for the synthesized catalysts.

Note S2. Radical kinetic fitting

For the decarboxylation reaction of phenylacetic acid over metal/TiO_2 catalyst, the generated benzyl radical can combine with surface hydrogen species to produce toluene, or undergo homo-coupling to yield bibenzyl. The former pathway is a first-order reaction for benzyl radical, while the latter is a second-order reaction for benzyl radical. The rate function of these two pathways can be described as follow:

$$\frac{dc}{dt} = k_1 c \qquad \text{(S5)}$$

$$\frac{dc}{dt} = k_2 c^2 \qquad \text{(S6)}$$

where k_1 and k_2 correspond to the rate constants of the first-order and the second-order reaction, respectively. Through a definite integral calculation, Equation S5 and S6 can be transformed into

$$c_t = c_0 \exp(-k_1 t) \qquad \text{(S7)}$$

$$c_t = \frac{1}{k_2 t + {}^1/_{c_0}} \qquad \text{(S8)}$$

where c_0 and c_t correspond to the initial concentration of radical species and the concentration at a specific reaction time, respectively. Both reaction pathways contribute to the conversion of radical intermediate. Thereby the total reaction rate function can be described as follow:

$$\frac{dc}{dt} = k_1 c + k_2 c^2 \qquad \text{(S9)}$$

The integral of Equation S9 leads to a very complicated function of c_t, which considerably hinders the subsequent data fitting. In this study, we define a kinetic weight coefficient ($0 \leq \boldsymbol{a} \leq 1$) to disclose the kinetic feature of radical reaction over metal/TiO_2 catalyst in a more straightforward manner. The mixed reaction kinetics can be given as follows:

$$c_t = a c_0 \exp(-k_1 t) + \frac{1-a}{k_2 t + {}^1/_{c_0}} \qquad \text{(S10)}$$

If $\boldsymbol{a}$ is close to 1, the second term on the right side, that is, the contribution of the second-order reaction pathway become negligible, and Equation S10 becomes analogous to the first-order kinetics function, Equation S7. In this situation, the radical reaction is expected to follow a pseudo-first-order kinetics. On the other hand, if $\boldsymbol{a}$ is close to 0, the second-order reaction pathway becomes dominant. Consequently, we can facilely reveal the corresponding kinetic tendency based on the obtained $\boldsymbol{a}$ value.

According to the Lambert-Beer law ($\Delta \mathrm{Abs}_t = c_t \varepsilon l$, where ε is the molar attenuation coefficient and l is the optical path length), Equation S10 can be transformed into

$$\Delta \mathrm{Abs}_t = a \Delta \mathrm{Abs}_0 \exp(-k_1 t) + \frac{1-a}{\frac{k_2}{\varepsilon l} t + {}^1/_{\Delta \mathrm{Abs}_0}} \qquad \text{(S11)}$$

With Equation S11 in hand, we can directly study the reaction kinetics of benzyl radical conversion over metal/TiO_2 catalyst from the obtained transient decay.

The transient decay over different metal/TiO_2 catalysts indeed can be well fitted with Equation S11, delivering the corresponding coefficient of fitting determination (R^2) ranging from 0.840 to 0.922 (Figure 2F-2J, Table S1). The obtained second-order rate constants do not vary markedly with different metal//TiO_2 catalysts. However, the first-order rate constant for Pd/TiO_2 is significantly smaller those for other metal/TiO_2 catalysts, which implies a different reaction mechanism for radical hydrogenation over Pd/TiO_2. This could be explained that the hydrogenation process over Pd catalyst may involve a surface-stabilized radical, while over other metal//TiO_2 catalysts the radical species tend to react as free radicals. It should be noted that the obtained rate constants in Table S1 are less meaningful because they derive from the deliberately defined kinetic function (Equation S10) instead of the real one (the integral equation of Equation S9). To obtain the exact rate constants of the radical reactions is not within the scope of our study. Instead, we want to disclose the distinct radical kinetic features among the selected metal/TiO_2 catalysts, and we find that Pd/TiO_2 displays a radical kinetics remarkably different from other metal/TiO_2 catalysts. For Pt, Au, Rh, and Ni catalyst, kinetic fitting with Equation S11 leads to moderate values of ***a*** ranging from 0.383 to 0.621, which indicates that both the combination with surface hydrogen species and homo-coupling are the are the major pathways for benzyl radical conversion over these metal/TiO_2 catalysts. The unspecific kinetics illustrates that radical species are prone to react in a free and uncontrolled manner. The kinetic weight coefficient slightly varies with different catalysts, probably due to the distinct physicochemical properties of different metal species. In contrast, kinetic fitting over Pd catalyst delivers an ***a*** value close to 1 (0.929), indicating a predominant first-order kinetics for radical conversion, which is completely different from the common free radical pathway. Consequently, we deduce that Pd nanoparticles would efficiently adsorb the free radical intermediates and transform them into surface-stabilized species, thereby making their combination with surface hydrogen species as their dominant conversion pathway.

Supplementary figures

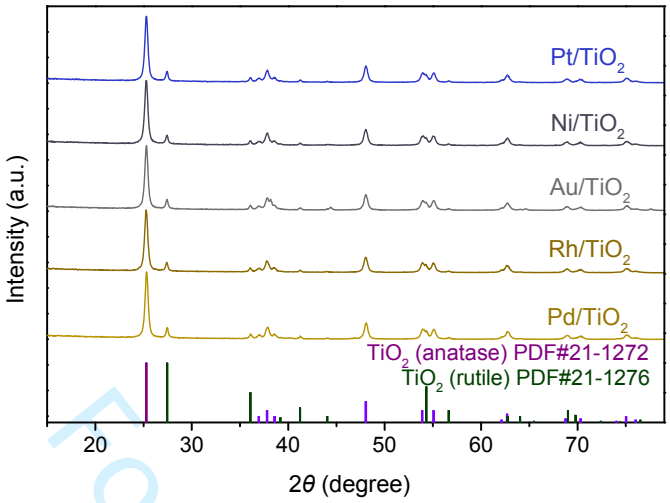

Figure S1. XRD patterns of metal/TiO_2 catalysts.

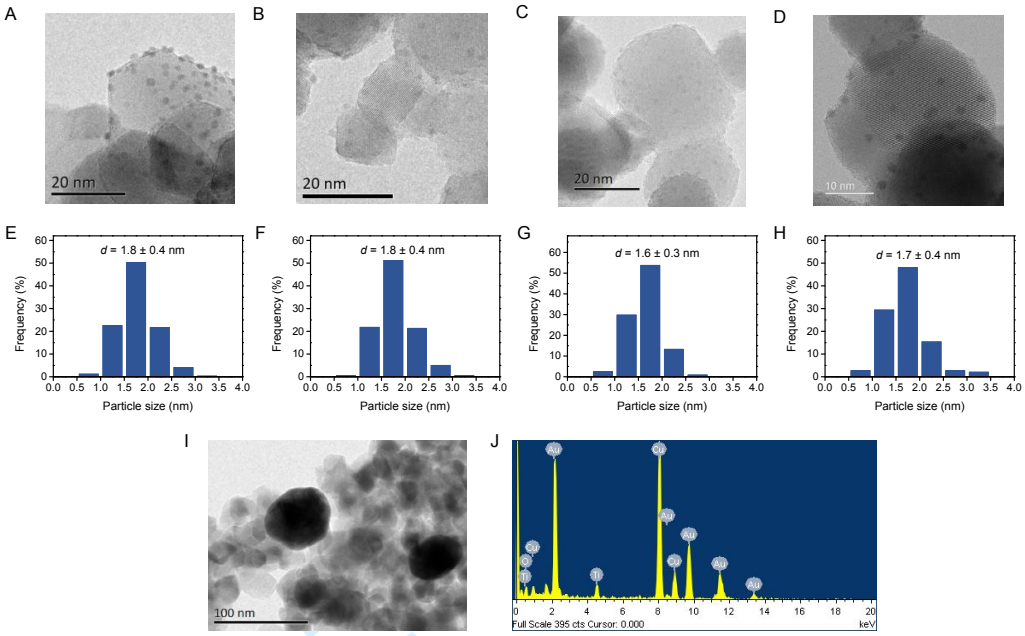

Figure S2. TEM image of (**A**) Pt/TiO_2, (**B**) Rh/TiO_2, (**C**) Ni/TiO_2, (**D**) Pd/TiO_2, and (**I**) Au/TiO_2. Size distribution of metal nanoparticles on (**E**) Pt/TiO_2, (**F**) Rh/TiO_2, (**G**) Ni/TiO_2, and (**H**) Pd/TiO_2 (based on more than 120 nanoparticles). (**J**) The EDX spectrum of Au/TiO_2.

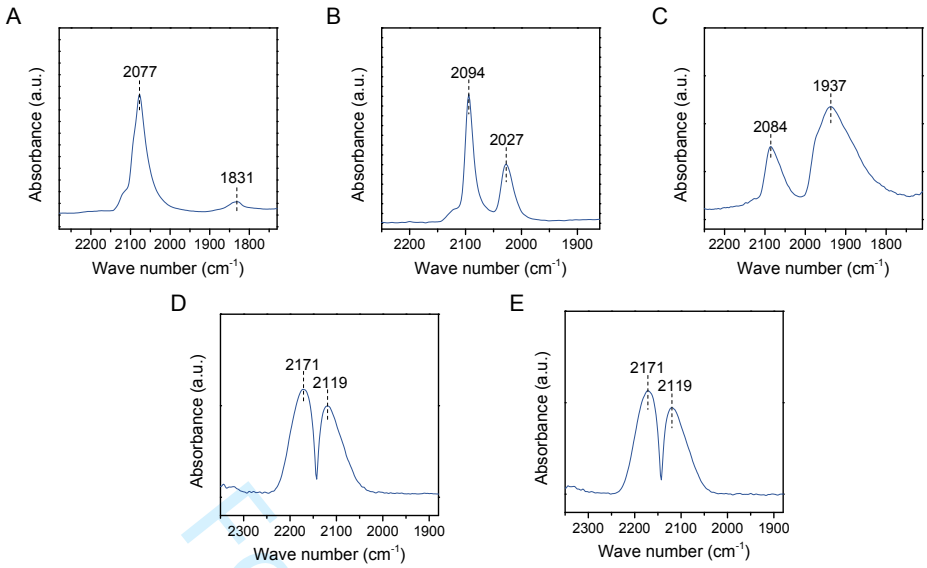

Figure S3. CO adsorption FT-IR spectra of (**A**) Pt/TiO_2, (**B**) Rh/TiO_2, (**C**) Pd/TiO_2, (**D**) Au/TiO_2, and (**E**) Ni/TiO_2 at room temperature.

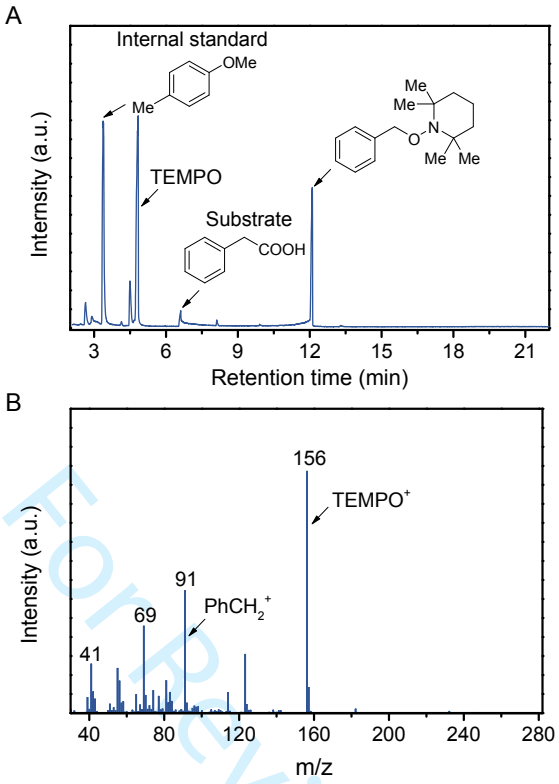

Figure S4. (**A**) GC-MS pattern of photocatalytic hydrodecarboxylation of phenylacetic acid with 2,2,6,6-tetramethylpiperidinooxy (TEMPO) (1.5 equiv.) over Pd/TiO_2 in an argon atmosphere. (**B**) MS spectra in GC-MS pattern at a retention time of 12.08 min.

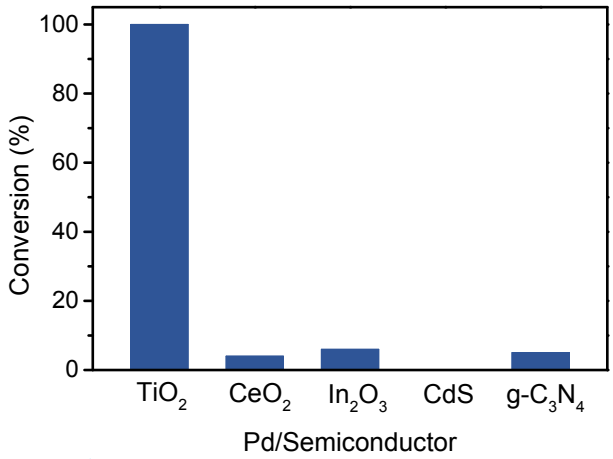

Figure S5. The conversion of phenylacetic acid over different Pd/semiconductor catalysts. Reaction conditions: Phenylacetic acid (0.15 mmol), photocatalyst (5 mg), acetonitrile (1.2 mL), Ar (0.1 MPa), room temperature (30 ± 5 °C), LEDs (356 nm, 18 W) irradiation for 3 h.

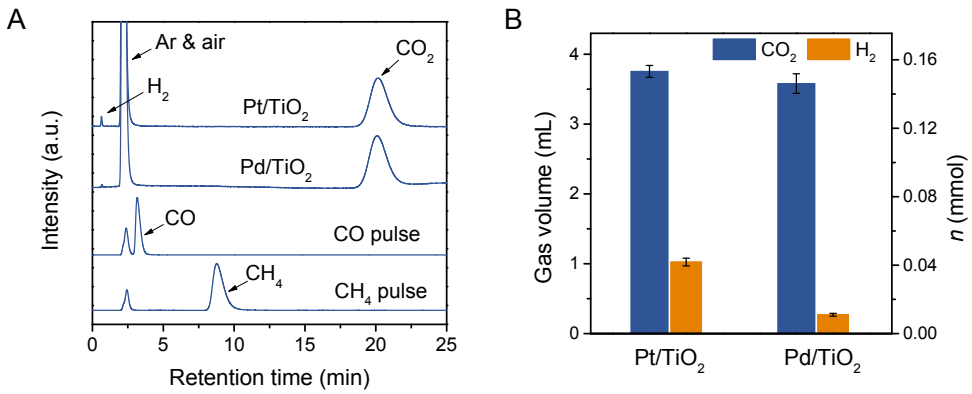

Figure S6. (**A**) GC patterns of gas products (**B**) the evolution amount of CO_2 and H_2 in the photocatalytic reactions of phenylacetic acid over Pt/TiO_2 and Pd/TiO_2 at a reaction time of 3 h in Ar atmosphere.

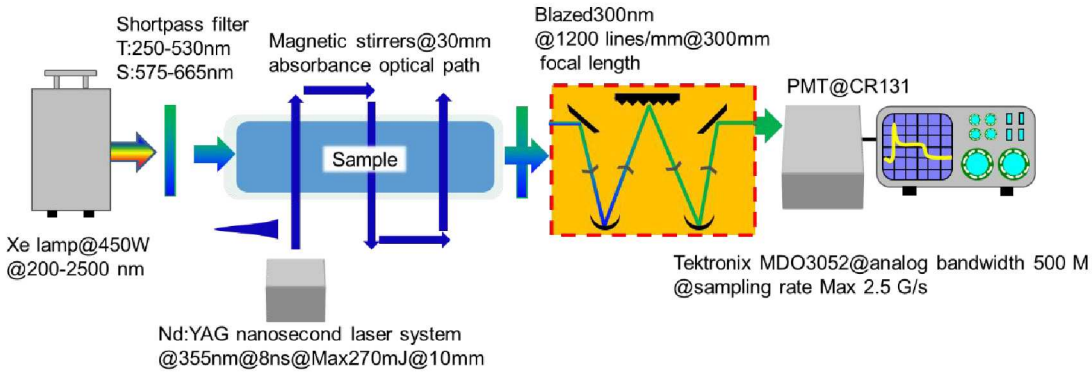

Figure S7. A schematic representation of TA spectrograph.

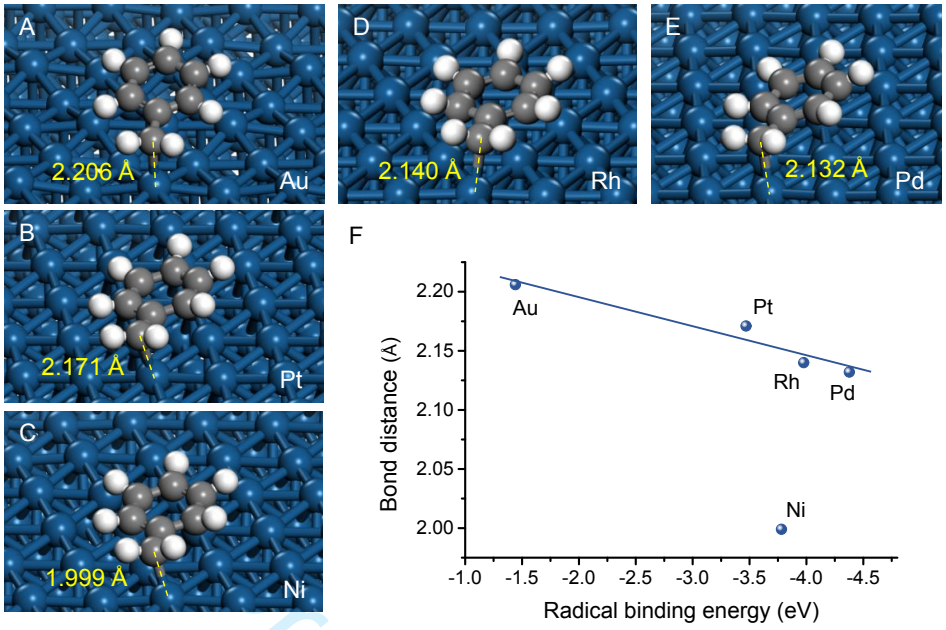

Figure S8. The optimal conformation of benzyl radical adsorption on (**A**) Au (111), (**B**) Pt (111), (**C**) Ni (111), (**D**) Rh (111), and (**E**) Pd (111), respectively. (**F**) The relationship between binding energy of benzyl radical and the bond distance of metal-benzyl carbon bond in the optimal conformations. The radical binding energy exhibits an almost linear dependence on the bond distance over noble metal catalysts (Au, Pt, Rh, and Pd). This relationship does not apply to Ni catalyst due to its markedly different electronic structure compared to the other four metals.

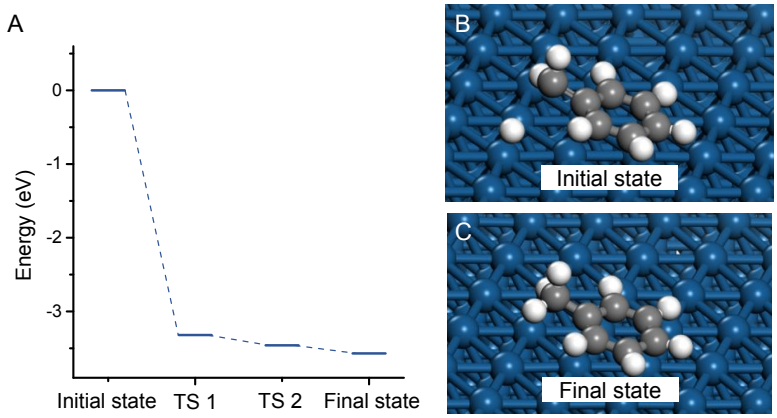

Figure S9. (**A**) The calculated energy profile for benzyl radical hydrogenation on Pd (111). The optimal conformation of the (**B**) initial state and (**C**) final state for benzyl radical hydrogenation on Pd (111). TS, transition state.

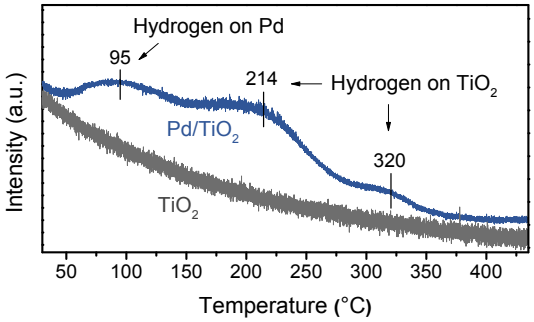

Figure S10. H_2-TPD profiles of Pd/TiO_2 and TiO_2 after exposure to H_2 at ambient temperature.

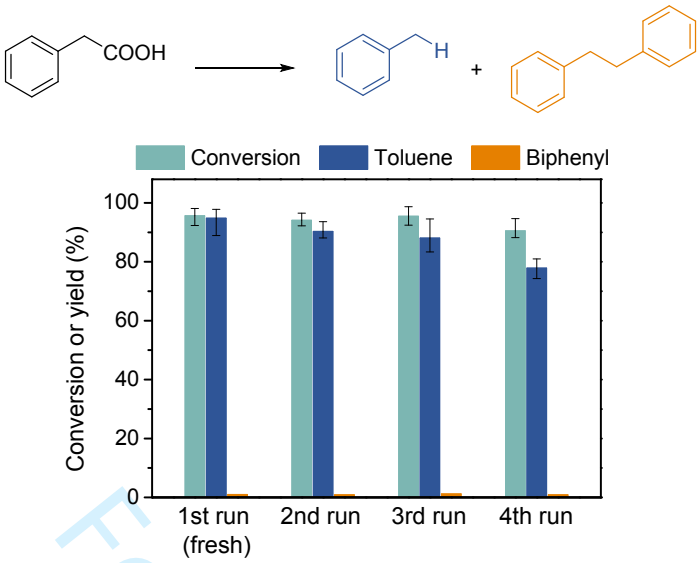

Figure S11. Cyclic test for phenylacetic acid conversion over Pd/TiO_2 in a H_2 atmosphere (0.1 MPa).

Supplement tables

Table S1. The results of mixed kinetic fitting for TA signal decay over metal/TiO_2 catalysts.

$$\triangle \mathrm{Abs}_t = a \ \triangle \mathrm{Abs}_0 \exp(-k_1 t) + \frac{1-a}{\frac{k_2}{\varepsilon l} t + 1/\triangle \mathrm{Abs}_0}$$

entry	catalyst	**a**	$\triangle Abs_0$	k_1 (μs^{-1})	$k_2/\varepsilon l$ (μs^{-1})	R^2
1	Pt/TiO_2	0.554±0.029	0.0143±0.0006	3.964±0.616	16.155±2.098	0.840
2	Au/TiO_2	0.490±0.032	0.0195±0.0006	3.770±0.545	20.569±2.246	0.922
3	Rh/TiO_2	0.383±0.040	0.0138±0.0007	5.213±1.409	26.063±2.811	0.855
4	Ni/TiO_2	0.621±0.019	0.0183±0.0006	3.983±0.392	11.396±1.215	0.901
5	Pd/TiO_2	0.929±0.338	0.0153±0.0005	0.665±0.142	9.815±86.324	0.875

Table S2. The results of first-order kinetic fitting for TA signal decay over metal/TiO_2 catalysts.

$$\triangle \mathrm{Abs}_t = \triangle \mathrm{Abs}_0 \exp(-k_1 t)$$

entry	catalyst	$\triangle Abs_0$	k_1 (μs^{-1})	R^2
1	Pt/TiO_2	0.0077±0.0002	0.196±0.010	0.674
2	Au/TiO_2	0.0113±0.0003	0.261±0.011	0.770
3	Rh/TiO_2	0.0086±0.0002	0.213±0.008	0.798
4	Ni/TiO_2	0.0090±0.0003	0.201±0.011	0.653
5	Pd/TiO_2	0.0148±0.0004	0.558±0.022	0.871

^{1}H and ^{13}C NMR spectra

^{1}H and ^{13}C NMR spectra were collected on a Bruker AVIII 400 spectrometer (^{1}H: 400 MHz and ^{13}C: 101 MHz). The tetramethylsilane (TMS) in the solvent of $CDCl_3$ was used as the internal standard (^{1}H NMR: TMS at 0.00 ppm, $CHCl^3$ at 7.22 ppm; ^{13}C NMR: $CHCl_3$ at 77.0 ppm).

Product **5**

The crude product was purified by preparative TLC using petroleum ether as eluent. Pure product **5** was obtained as a white solid in 93% yield. Following are the **1**H NMR and ^{13}C NMR spectra of **5**, respectively. ^{1}H NMR (400 MHz, $CDCl_3$) δ = 7.57 (d, *J* = 7.6, 2H), 7.49 (d, *J* = 8.0, 2H), 7.41 (t, *J* = 7.6, 2H), 7.31 (t, *J* = 7.6, 1H), 7.24 (d, *J* = 8.0, 2H), 2.39 (s, 3H). ^{13}C NMR (176 MHz, $CDCl_3$) δ = 141.21, 138.40, 137.05, 129.52, 128.75, 127.03, 127.01, 21.14.

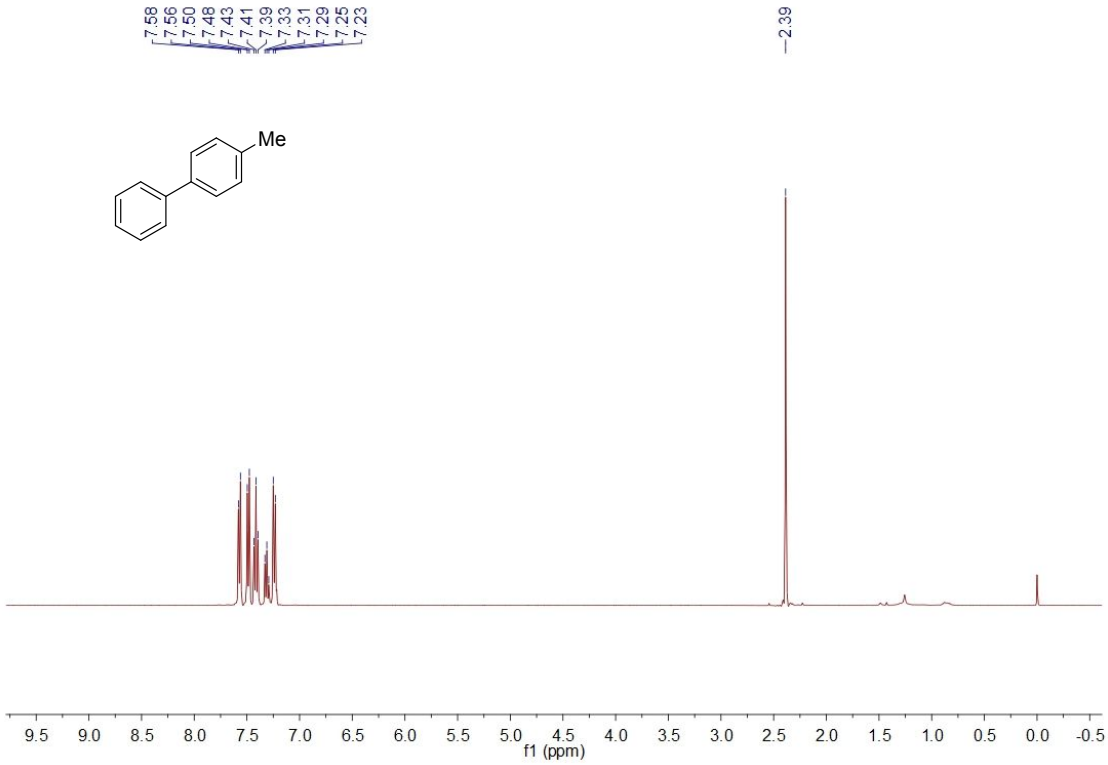

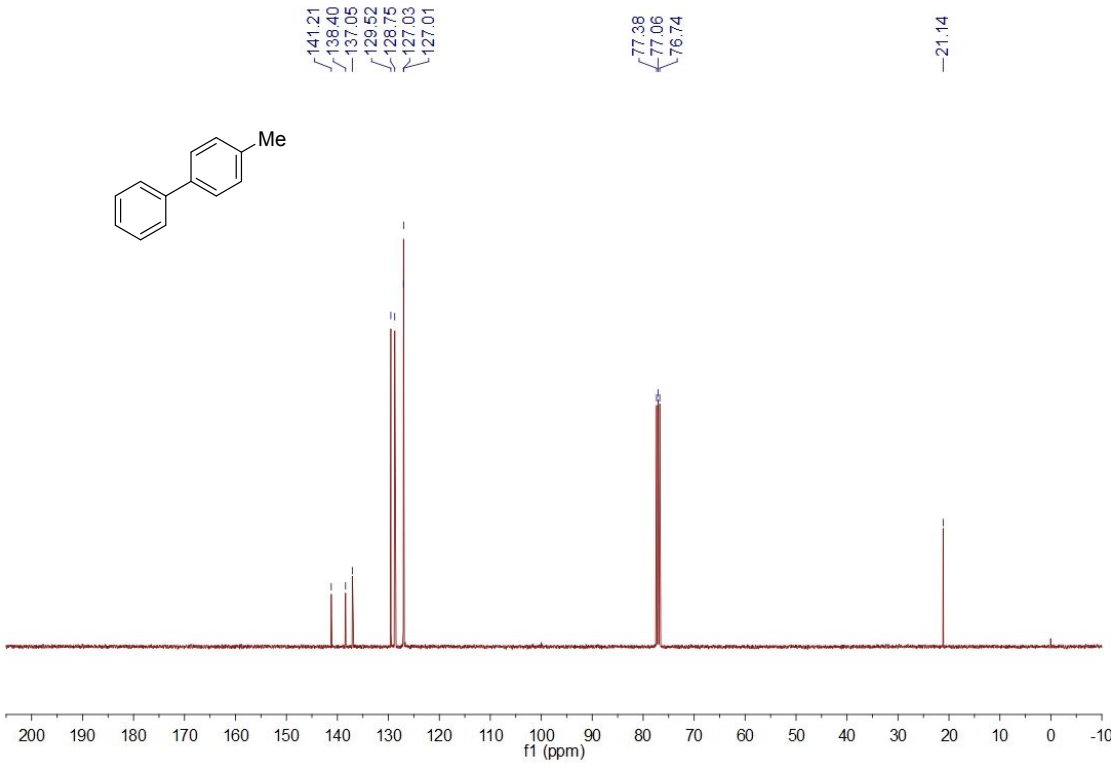

Product **21**

The crude product was purified by preparative TLC using petroleum ether as eluent. Pure product **21** was obtained as a colorless liquid in 84% yield. Following are the ^{1}H NMR and ^{13}C NMR spectra of **21**, respectively. ^{1}H NMR (400 MHz, $CDCl_3$) δ = 7.29-7.17 (m, 10H), 3.97 (s, 2H). ^{13}C NMR (176 MHz, $CDCl_3$) δ = 141.17, 128.99, 128.51, 126.12, 42.00.

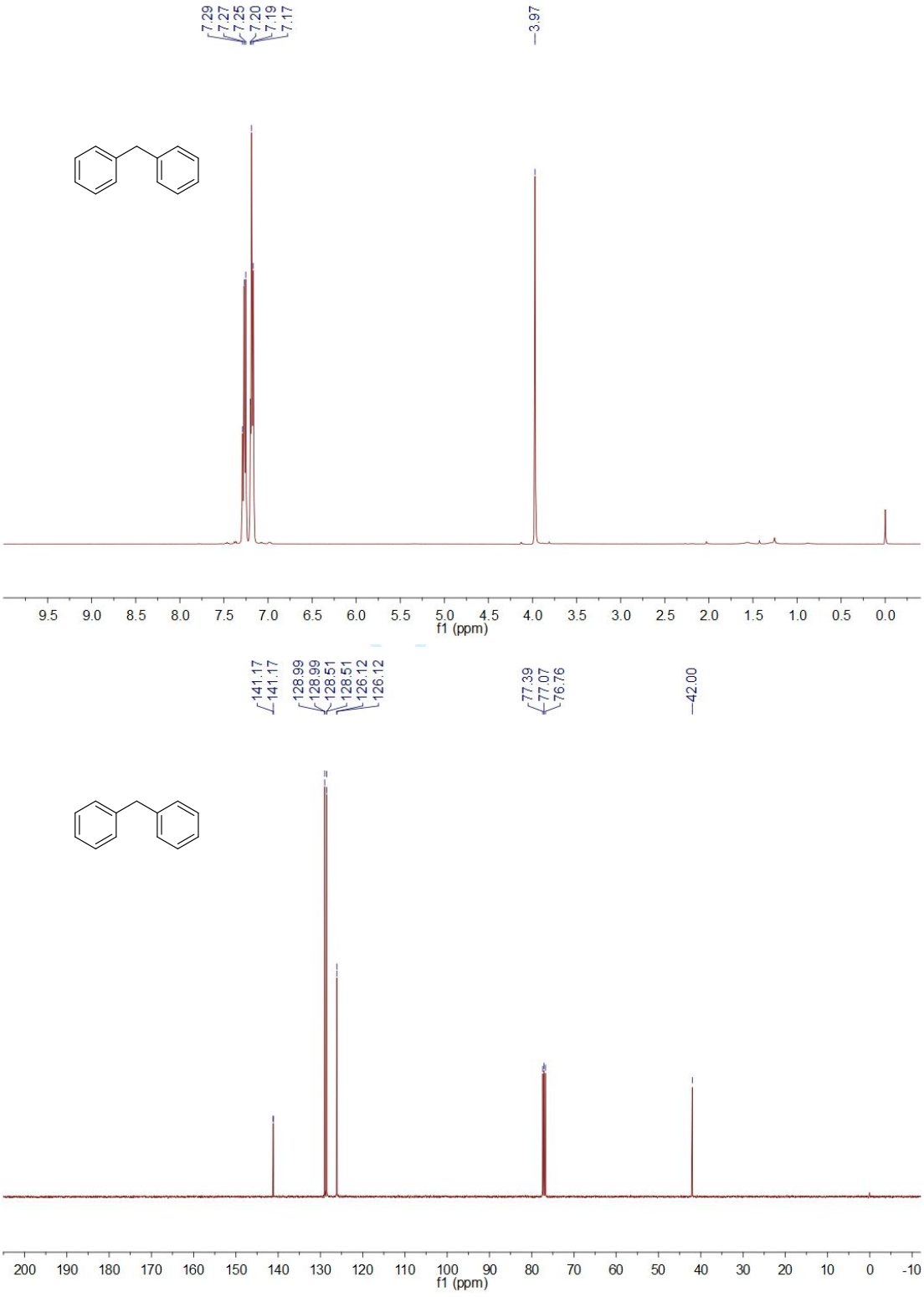

Product **26**

The crude product was purified by preparative TLC using petroleum ether as eluent. Pure product **26** was obtained as a pale yellow liquid in 91% yield. Following are the ^{1}H NMR and

^{13}C NMR spectra of **26**, respectively. ^{1}H NMR (400 MHz, $CDCl_3$) δ = 7.55-7.52 (m, 2H), 7.44-7.40 (m, 2H), 7.44-7.40 (m, 2H), 7.36-7.35 (m, 2H), 7.04-6.97 (m, 2H), 2.67 (q, *J* = 7.6, 2H), 2.67 (q, *J* = 7.6, 2H), 1.26 (t, *J* = 7.6, 3H). ^{13}C NMR (176 MHz, $CDCl_3$) δ = 160.99, 158.53, 145.98, 145.90, 135.99, 135.98, 135.99, 135.98, 130.52, 130.48, 129.00, 128.97, 128.42, 127.41, 128.31, 126.18, 123.90, 123.86, 115.50, 115.28, 28.41, 28.39, 15.27.

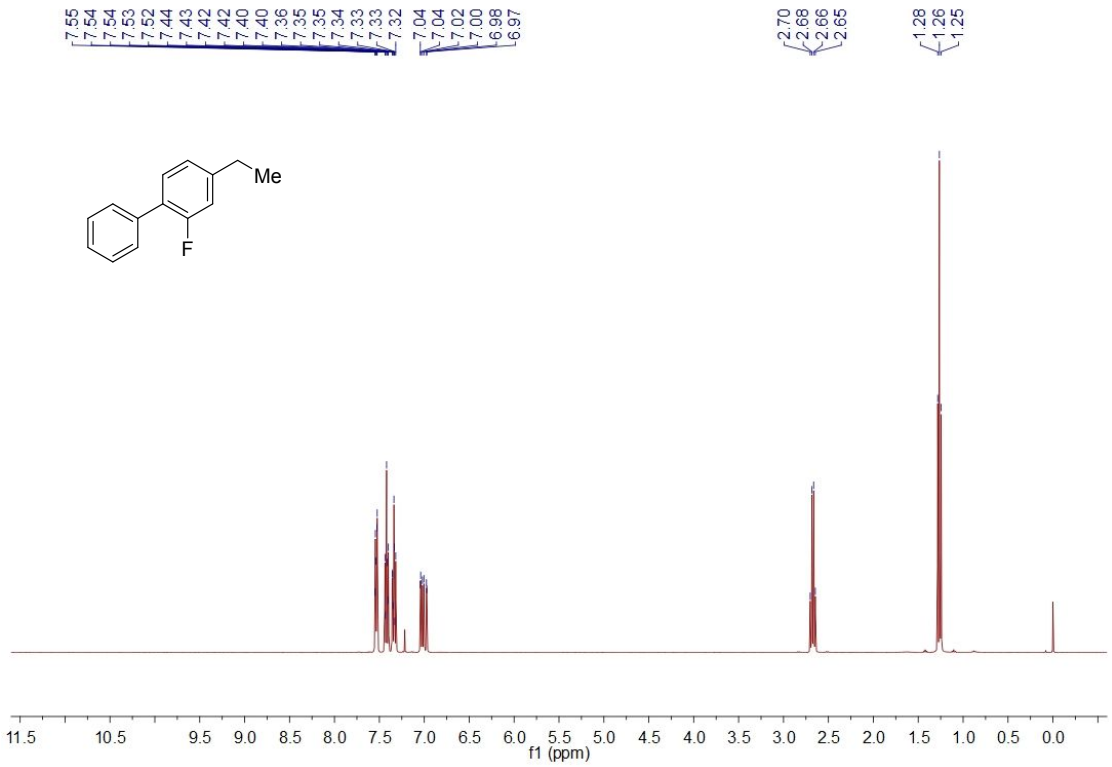

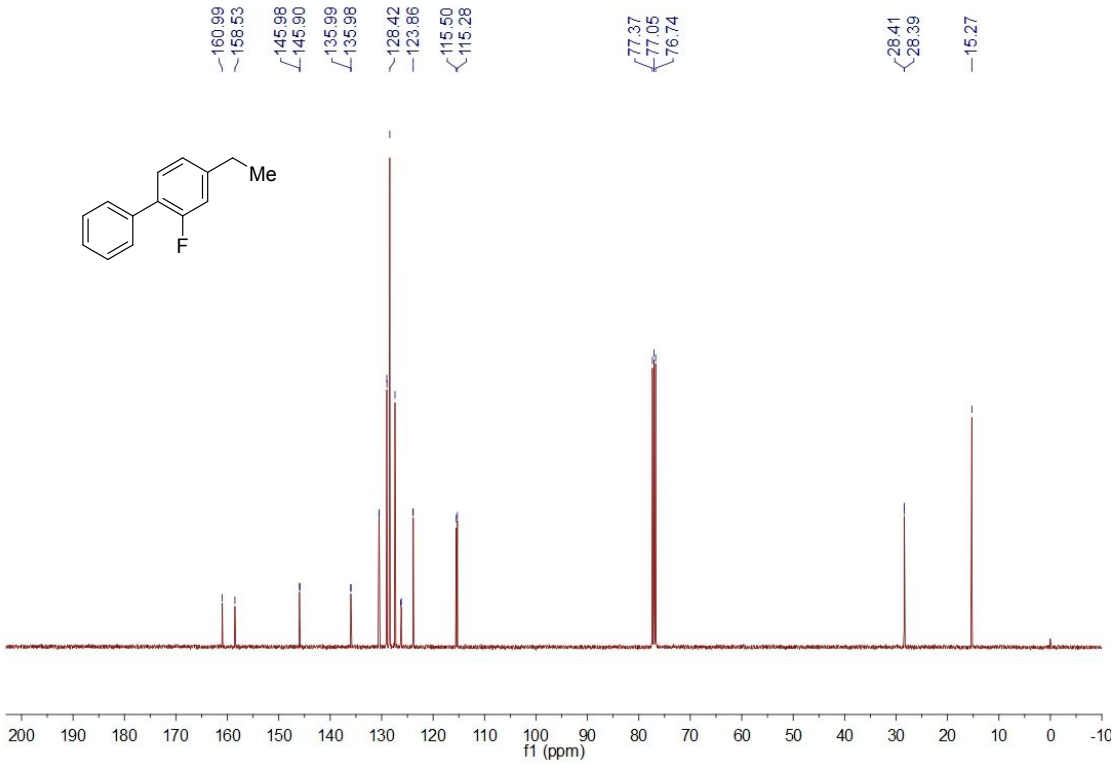

Product **27**

The crude product was purified by preparative TLC using ethyl acetate: petroleum ether = 1:10 as eluent. Pure product **27** was obtained as a white solid in 90% yield. Following are the ^{1}H NMR and ^{13}C NMR spectra of **27**, respectively. ^{1}H NMR (400 MHz, $CDCl_3$) δ = 7.68-7.65 (m, 2H), 7.55 (s, 1H), 7.31 (dd, J = 8.4, 1.2, 1H), 7.13-7.10 (m, 2H), 3.91 (s, 3H), 2.78 (q, J = 7.6, 2H), 1.31 (t, J = 7.6, 3H). ^{13}C NMR (176 MHz, $CDCl_3$) δ = 157.09, 139.46, 132.90, 129.18, 128.90, 127.55, 126.69, 125.42, 118.59, 105.68, 55.29, 28.83, 15.62.

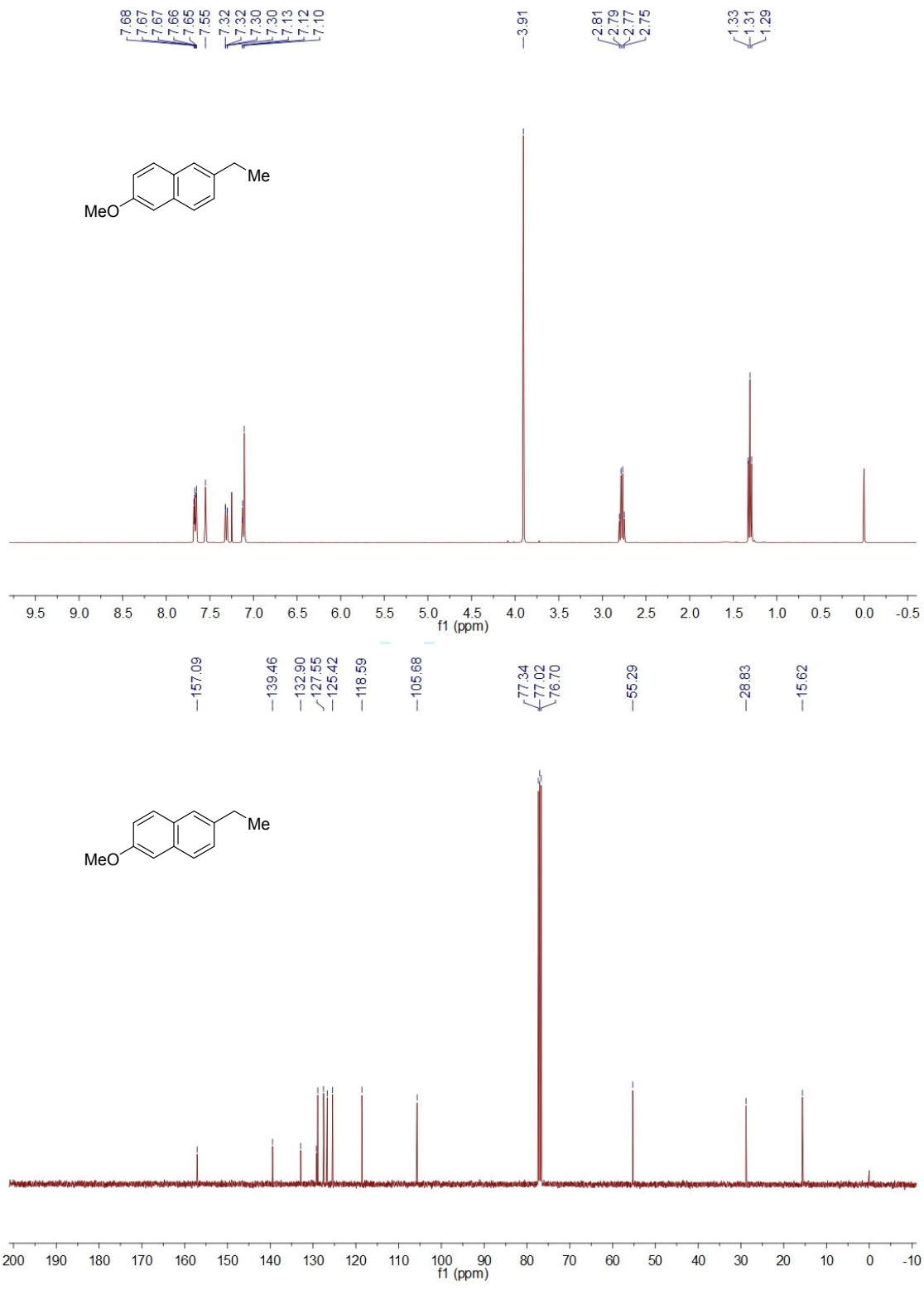
7.68
7.67
7.67
7.66
7.65
7.55
7.32
7.32
7.30
7.30
7.13
7.12
7.10
3.91
2.81
2.79
2.77
2.75
1.33
1.31
1.29
Me
MeO
f1 (ppm)
157.09
139.46
132.90
127.55
125.42
118.59
105.68
77.34
77.02
76.70
55.29
28.83
15.62
Me
MeO
f1 (ppm)

References

[1] Y. Wang, F. Wang, Q. Song, Q. Xin, S. Xu, J. Xu, *J. Am. Chem. Soc.*, **2013**, 135, 1506-1515.

[2] L. B. Hoch, T. E. Wood, P. G. O'Brien, K. Liao, L. M. Reyes, C. A. Mims, G. A. Ozin, *Adv. Sci.*, **2014**, 1, 1400013.

[3] J. S. Jang, U. A. Joshi, J. S. Lee, *J. Phys. Chem. C*, **2007**, 111, 13280-13287.

[4] Y. Yang, L. Liu, J. Chen, K. Han, *Phys. Chem. Chem. Phys.*, **2014**, 16, 17828-34.

[5] Y. Yang, J.-S. Chen, J.-Y. Liu, G.-J. Zhao, L. Liu, K.-L. Han, T. R. Cook, P. J. Stang, *J. Phys. Chem. Lett.*, **2015**, 6, 1942-1947.

[6] J. Schneider, D. Bahnemann, *J. Phys. Chem. C*, **2018**, 122, 13979-13985.

[7] N. Luo, T. Montini, J. Zhang, P. Fornasiero, E. Fonda, T. Hou, W. Nie, J. Lu, J. Liu, M. Heggen, L. Lin, C. Ma, M. Wang, F. Fan, S. Jin, F. Wang, *Nat. Energy*, **2019**, 4, 575-584.

[8] K. Jeništová, I. Hachemi, P. Mäki-Arvela, N. Kumar, M. Peurla, L. Čapek, J. Wärnå, D. Y. Murzin, *Chem. Eng. J.*, **2017**, 316, 401-409.

[9] J. P. Perdew, K. Burke, M. Ernzerhof, *Phys. Rev. Lett.*, **1996**, 77, 3865-3868.

[10] G. Kresse, J. Furthmüller, *Comput. Mater. Sci.*, **1996**, 6, 15-50.

[11] P. E. Blöchl, *Phys. Rev. B*, **1994**, 50, 17953-17979.

[12] G. Kresse, D. Joubert, *Phys. Rev. B*, **1999**, 59, 1758-1775.

[13] G. Kresse, J. Furthmüller, *Phys. Rev. B*, **1996**, 54, 11169-11186.

[14] S. Grimme, J. Antony, S. Ehrlich, H. Krieg, *J. Chem. Phys.*, **2010**, 132, 154104.

[15] Y. Li, P. Ren, D. Zhang, W. Qiao, D. Wang, X. Yang, X. Wen, M. H. Rummeli, H. Niemantsverdriet, J. P. Lewis, F. Besenbacher, H. Xiang, Y. Li, R. Su, *ACS Catal.*, **2021**, 11, 4338-4348.

[16] J. Heyd, G. E. Scuseria, *J. Chem. Phys.*, **2003**, 118, 8207-8215.

[17] T. D. Kühne, M. Iannuzzi, M. D. Ben, V. V. Rybkin, P. Seewald, F. Stein, T. Laino, R. Z. Khaliullin, O. Schütt, F. Schiffmann, D. Golze, J. Wilhelm, S. Chulkov, M. H. Bani-Hashemian, V. Weber, U. Borštnik, M. Taillefumier, A. S. Jakobovits, A. Lazzaro, H. Pabst, T. Müller, R. Schade, M. Guidon, S. Andermatt, N. Holmberg, G. K. Schenter,

A. Hehn, A. Bussy, F. Belleflamme, G. Tabacchi, A. Glöß, M. Lass, I. Bethune, C. J. Mundy, C. Plessl, M. Watkins, J. VandeVondele, M. Krack, J. Hutter, *J. Chem. Phys.*, **2020**, 152, 194103.

[18] P. Panagiotopoulou, D. I. Kondarides, *Appl. Catal., B*, **2011**, 101, 738-746.

[19] J. Raskó, Z. Szabó, T. Bánsági, F. Solymosi, *Phys. Chem. Chem. Phys.*, **2001**, 3, 4437-4443.

[20] Q. Fan, S. He, L. Hao, X. Liu, Y. Zhu, S. Xu, F. Zhang, *Sci. Rep.*, **2017**, 7, 42172.

[21] J. Wan, W. Chen, C. Jia, L. Zheng, J. Dong, X. Zheng, Y. Wang, W. Yan, C. Chen, Q. Peng, D. Wang, Y. Li, *Adv. Mater.*, **2018**, 30, 1705369.

[22] M. Mihaylov, K. Chakarova, K. Hadjiivanov, *J. Catal.*, **2004**, 228, 273-281.